

GAUSSIAN PEAKS AND CLUSTERS OF GALAXIES

RENYUE CEN¹

Draft version March 6, 2018

ABSTRACT

We develop and test a method to compute mass and auto-correlation functions of rich clusters of galaxies from linear density fluctuations, based on the formalism of Gaussian peaks (Bardeen et al. 1986). The essential, new ingredient in the current approach is a simultaneous and unique fixture of the *size* of the smoothing window for the density field, r_f , and the *critical height* for collapse of a density peak, δ_c , for a given cluster mass (enclosed within the sphere of a given radius rather than the virial radius, which is hard to measure observationally). Of these two parameters, r_f depends on both the mass of the cluster in question and Ω , whereas δ_c is a function of only Ω and Λ . These two parameters have formerly been treated as adjustable and approximate parameters. Thus, for the first time, the Gaussian Peak Method (GPM) becomes unambiguous, and more importantly, accurate, as is shown here.

We apply this method to constrain all variants of the Gaussian cold dark matter (CDM) cosmological model using the observed abundance of local rich clusters of galaxies and the microwave background temperature fluctuations observed by COBE. The combined constraint fixes the power spectrum of any model to $\sim 10\%$ accuracy in both the shape and overall amplitude. To set the context for analyzing CDM models, we choose six representative models of current interest, including an $\Omega_0 = 1$ tilted cold dark matter model, a mixed hot and cold dark matter model with 20% mass in neutrinos, two lower density open models with $\Omega_0 = 0.25$ and $\Omega_0 = 0.40$, and two lower density flat models with $(\Omega_0 = 0.25, \Lambda_0 = 0.75)$ and $(\Omega_0 = 0.40, \Lambda_0 = 0.60)$. This suite of CDM models should bracket any CDM model that is currently viable. The parameters of all these models are also consistent with a set of other constraints, including the Hubble constant, the age of the universe and the light-element nucleosynthesis with Ω_b chosen to maximize the viability of each model with respect to the observed gas fraction in X-ray clusters.

Subject headings: Cosmology: large-scale structure of Universe – cosmology: theory – galaxies: clustering – galaxies: formation – numerical method

1. INTRODUCTION

Clusters of galaxies are cosmologically important because they contain vitally important information on scales from a few megaparsecs to several hundred megaparsecs, and provide fossil evidence for some of the basic cosmological parameters (Richstone, Loeb, & Turner 1992; Bahcall, Fan, & Cen 1997). The fact that they are among the most luminous objects in the universe renders them an effective and economical tracer of the large-scale structure, not only of the local universe (Bahcall 1988) but also of the universe at moderate-to-high redshift.

Perhaps more interesting is the fact that clusters of galaxies are intrinsically rare with typical separations of $\sim 50h^{-1}$ Mpc at $z \sim 0$ and seemingly rarer at high redshift (Luppino & Gioia 1995; Carlberg et al. 1996; Postman et al. 1996). Their rarity is traceable to the fact that they only form at the rare, high peaks in the initial density field. Since the mass in a sphere of radius $10h^{-1}$ Mpc roughly corresponds to the mass of a rich cluster like the Coma cluster, the abundance of clusters of galaxies (i.e., the cluster mass function, Bahcall & Cen 1992) provides a sensitive test of the amplitude of the density fluctuations on that scale and places one of the most stringent constraints on cosmological models to date (Peebles, Daly, & Juskiewicz 1989; Henry & Arnaud 1991; Bahcall & Cen 1992; Oukbir & Blanchard 1992; Bartlett & Silk 1993; White et al. 1993a, WEF henceforth; Viana & Liddle 1996; Eke, Cole & Frenk 1996, ECF henceforth; Pen 1996)

The spatial distribution of clusters of galaxies provides complementary information for cosmological models. A widely used statistic for clusters of galaxies is the two-point auto-correlation function. Earlier pioneering work (Bahcall & Soneira 1983; Klypin & Kopylov 1983) has met with dramatic improvements in recent years thanks to larger and/or new cluster samples that have become available (Postman, Huchra, & Geller 1992; Nichol et al. 1992; Dalton et al. 1992,1994; Romer et al. 1994; Croft et al. 1997). Comparing with cosmological models clearly show that the two-point correlation function of clusters of galaxies provides a strong test on cosmological models on scales from several tens to several hundred megaparsecs (Bardeen, Bond, & Efstathiou 1987; Bahcall & Cen 1992; Mann, Heavens, & Peacock 1993; Holtzman & Primack 1993; Croft & Efstathiou 1994; Borgani et al. 1995). In addition, the recent studies of superclusters and supervoids by Einasto et al. (1997a,b,c) show a very intriguing property that the correlation function of rich clusters appears to be oscillatory on large scales. If confirmed, this would challenge most models.

Hence, the combination of cluster mass and correlation functions provides a critical constraint on cosmological models on scales $\geq 10 h^{-1}$ Mpc. While uncertainties remain in the current clustering analyses as well as the abundance of observed clusters due chiefly to still limited cluster sample sizes typically of order of a few hundred clusters, large surveys underway such as the Sloan Digital

¹Princeton University Observatory, Princeton University, Princeton, NJ 08544; cen@astro.princeton.edu

Sky Survey (SDSS; Knapp, Lupton, & Strauss 1996) and 2dF galaxy redshift survey (Colless 1998) should provide much more accurate determinations of both.

The groundwork for the gravitational instability picture of cluster formation was laid down more than two decades ago (Gunn & Gott 1972). In the context of Gaussian cosmological models, Kaiser (1984), in a classic paper, put forth the “biased” structure formation mechanism, where clusters of galaxies were predicted (correctly) to form at high peaks of the density field to explain the enhanced correlation of Abell clusters over that of galaxies. This idea was subsequently extended to objects on other scales including galaxies and the properties of linear Gaussian density fields were worked out in exquisite detail (Peacock & Heavens 1985; Bardeen et al. 1986, BBKS hereafter).

While alternatives exist (e.g., Zel’dovich 1980; Vilenkin 1981, 1985; Turok 1989; Barriola & Vilenkin 1989; Bennett & Rhie 1990), a Gaussian model is simple and attractive (largely because of it) in that all its properties can be fully specified by one single function, the power spectrum of its density fluctuations. Moreover, it is predicted that random quantum fluctuations generated in the early universe naturally produced Gaussian density fluctuations, whose scales were then stretched to the scales of cosmological interest by inflation (Guth & Pi 1982; Albrecht & Steinhardt 1982; Linde 1982; Bardeen, Steinhardt & Turner 1983). Furthermore, observations of large-scale structure and microwave background fluctuations appear to favor a Gaussian picture (Vogeley et al. 1994; Baugh, Gaztanaga, & Efstathiou 1995; Kogut et al. 1996; Colley, Gott, & Park 1996; Protogeris & Weinberg 1997; Colley 1997). So motivated, the present study will focus on the family of Gaussian CDM models. The reader is referred to Cen (1997c) for a discussion of the cluster correlation function in non-Gaussian models. We will employ the formalism of BBKS of Gaussian density field to devise an analytic method that can be used to directly compute the mass and correlation functions of clusters of galaxies. The needed input are: P_k (the power spectrum), Ω_0 and Λ_0 . The method developed is calibrated and its accuracy checked by a large set of N-body simulations.

The motivation for having such an analytic method is not only of an economical consideration (fast speed and much larger parameter space coverage possible) but also a necessity, especially for studying very rich clusters. For example, for clusters of mean separation of $200h^{-1}\text{Mpc}$ (about richness 3 and above; Bahcall & Cen 1993, BC henceforth), a simulation box of size $1170h^{-1}\text{Mpc}$ on a side would contain 200 such clusters, a number which may be required for reasonably sound statistical calculations. Assuming that the mass of such a cluster is $1.0 \times 10^{15}h^{-1}M_\odot$ (approximately the mass of a richness 3 cluster; BC) and one requires 500 particles to claim an adequate resolution of the cluster, it demands a requisite particle mass of $2.0 \times 10^{12}h^{-1}M_\odot$. This particle mass requirement dictates that one discretize the whole simulation box into $10^{8.3}\Omega_0$ particles (Ω_0 is the density parameter of a model). Meantime, a minimum nominal spatial resolution of $0.5h^{-1}\text{Mpc}$ is needed to properly compute just the cluster mass within Abell radius of $1.5h^{-1}\text{Mpc}$, which translates to a spatial dynamic range of 2340. The combined spatial and mass resolution requirements are formidable for either PM code, which requires a very large mesh (2340^3) thus needs more

than 57GB of RAM to allow for such a large simulation and hence is very expensive, if possible, or an adaptive code such as P³M (Efstathiou et al. 1985) or TPM code (Xu 1995), where CPU cost will be prohibitively large even if RAM permits.

The paper is organized as follows. Descriptions of GPM for computing cluster mass function are presented in §2.1. Descriptions of GPM for computing the cluster correlation function are presented in §2.2. A calibration of Press-Schechter method using the fitted GPM parameters and some comparisons between GPM and Press-Schechter method are presented in §2.3. We discuss the various factors that affect the cluster mass function in §3. Detailed constraints by the local rich clusters and the COBE observations (Smoot et al. 1992) on all CDM models are presented in §4. A simple $\sigma_8 - \Omega_0$ relation (with errorbars) for CDM models is presented in §5, derived from fitting to the observed local cluster abundance alone. Conclusions are given in §6.

2. GAUSSIAN PEAK METHOD FOR CLUSTERS OF GALAXIES

2.1. Gaussian Peak Method for Cluster Mass Function

It is convenient to define some frequently used symbols first. Hubble constant is $H = 100h\text{km/s/Mpc}$. Ω_0 and Λ_0 are the density parameters due to non-relativistic matter and cosmological constant, respectively, at redshift $z = 0$. Ω_z and Λ_z are the same parameters at redshift z . r_A is the comoving radius of a sphere in units of $h^{-1}\text{Mpc}$, which in most times represents the Abell radius with value 1.5. r_v is the virial radius in comoving $h^{-1}\text{Mpc}$. r_f is the radius of a smoothing window in comoving $h^{-1}\text{Mpc}$. M_A is the mass within a sphere of radius r_A in units of $h^{-1}M_\odot$. M_v is the mass within a sphere of radius r_v (virial mass of a halo) in units of $h^{-1}M_\odot$. For formulae related to Gaussian density field we will follow the notation of BBKS throughout this paper.

The cluster mass function may be derived by relating the initial density peaks to the final collapsed clusters, provided that *peaks do not merge*. Two pieces of observations suggest that merger of initial density peaks of cluster size be infrequent. First, the typical separation between clusters of galaxies is $\sim 100 h^{-1}\text{Mpc}$, while the typical size of a cluster is $\sim 1 h^{-1}\text{Mpc}$. Second, empirical evidence of matter fluctuations, as indicated by observed galaxy number fluctuations (Davis & Peebles 1983; Strauss & Willick 1995), suggests that the current nonlinear scale is $\sim 8 h^{-1}\text{Mpc}$, which is just about the size of fluctuations that collapse to form clusters of galaxies; i.e., the majority of clusters of galaxies form at low redshift. However, a more quantitative argument, that merger rate should be small, can be made as follows. Suppose that a cluster is moving at velocity v_0 at $z = 0$, then we can compute the total comoving distance that the cluster has travelled in its entire lifetime as

$$d_{cm} = \int_0^{t_0} v_0 f(t)(1+z)dt, \quad (1)$$

where t_0 is the current age of the universe, $f(t)$ is a function to describe the evolution of the (proper) peculiar velocity of the cluster and the last term $(1+z)$ relates comoving distance to proper distance. To illustrate the point

we will first use $\Omega_0 = 1$, which gives the following simple relation:

$$d_{cm} = v_0 H_0. \quad (2)$$

To arrive to the above relation we have used the following simple relations: $t = t_0(1+z)^{-3/2}$, $t_0 = 2H_0^{-1}/3$, $f(z) = (1+z)^{-1/2}$ (linear growth rate of proper peculiar velocities; Peebles 1980). For any reasonable model clusters of galaxies do not move at a speed (peculiar velocity) much higher than $\sim 1000\text{km/s}$ at present (Cen, Bahcall & Gramann 1994); it can be obtained approximately in linear theory by integrating a power spectrum, smoothed by an appropriate window, to yield the total kinetic energy (e.g., Suto, Cen, & Ostriker 1992). Note that some galaxy in a virialized cluster may move at a higher speed, but we are not considering such objects. So, a cluster moving at 1000km/s today moves a total comoving distance of $10h^{-1}\text{Mpc}$ in an $\Omega_0 = 1$ universe. The same cluster will move a longer distance in a low Ω_0 universe, but not by a large factor. An upper bound on d_{cm} in such cases may be obtained by setting $\Omega_0 = 0$, in which case we have $f(z) = (1+z)$, $t_0 = H_0^{-1}$ and $t = t_0(1+z)^{-1}$. The upper bound is

$$d_{cm,ub} = v_0 H_0 (1 + z_{max}), \quad (3)$$

where z_{max} is the maximum redshift to which $\Omega = 0$ applies. Let us make a simple, approximate estimate for a realistic lower bound by taking $\Omega_0 = 0.2$, as follows. For an $\Omega_0 = 0.2$ model, the redshift at which $\Omega = 0.5$ is 3.0, which we denote as z_{max} . We treat the redshift range $z > z_{max}$ as an $\Omega = 1$ model and treat $z < z_{max}$ as an $\Omega = 0$ model, which gives a simple result:

$$d_{cm} = v_0 H_0 [(1 + z_{max}) + 1]. \quad (4)$$

For $z_{max} = 3.0$, $d_{cm} = 5v_0 H_0$. Since velocity decayed from z_{max} to $z = 0$, a more reasonable upper bound on v_0 is $1000/(1 + z_{max})\text{km/s}$. This gives $12.5h^{-1}\text{Mpc}$ for $v_0 = 1000\text{km/s}$ and $z_{max} = 3$.

Since one needs to collapse a sphere of $9.5\Omega_0^{-1/3}h^{-1}\text{Mpc}$ in a uniform density field to form a massive cluster of mass $1 \times 10^{15}h^{-1}M_\odot$, i.e., cluster density peaks have to have a separation of at least $\sim 20\Omega_0^{-1/3}h^{-1}\text{Mpc}$ and more likely $\sim 50h^{-1}\text{Mpc}$ (mean separation of rich clusters today), it thus seems quite unlikely that a significant fraction of any massive cluster peaks have merged by $z = 0$. This conclusion is, however, not in conflict with observations that seem to show signs of recent and/or ongoing merger activity. In general, merger is an ever-going processes (at least in the past) in any plausible (i.e., a plausible range in Ω_0) hierarchical structure formation model. But, these mergers or substructures seen in some clusters are sub rich cluster scale mergers, i.e., sub-peaks within a large cluster scale peak are in the process of merging, a result which is in fact expected if clusters have been forming in the recent past in a hierarchical fashion. To our knowledge, there is no major merger event of two massive clusters observed. For example, in 55 Abell clusters catalogued by Dressler (1980), there is no case of two massive clusters in the process of imminent merging, although there does seem to have significant substructures in a significant fraction of clusters in various optical studies (e.g., Geller & Beers 1982; Dressler & Shectman 1988; West, Oemler, & Dekel 1988). X-ray observations also show a large fraction of

clusters with substructures (see Forman & Jones 1994 for a review). That being said, one needs to be extra cautious in interpreting such sub cluster scale merger/substructure events, due to unavoidable projection contaminations (see Cen 1997 for a thorough discussion of projection effects).

Having shown that merger should be infrequent, the key link then is to relate a density peak of height

$$\nu = F/\sigma_0 \quad (5)$$

to the final mass of a cluster defined within a fixed radius, say, the Abell radius r_A . Here, F is a density field smoothed by a window of size r_f and σ_0 is the rms fluctuation of F . Gaussian smoothing window (in Fourier space)

$$W(kr_f) = \exp(-r_f^2 k^2/2), \quad (6)$$

will be used throughout this paper, because it guarantees convergence of any spectral moment integral with any plausible power spectrum. Top-hat smoothing does not have this feature. For the sake of definiteness and convenience in comparing with observations, we define a cluster mass, M_A , as the mass in a sphere of *comoving* Abell radius, $r_A = 1.5h^{-1}\text{Mpc}$, in most cases. Cluster mass defined otherwise will be noted in due course. But the formalism developed here should be applicable for any plausible radius.

For a spherical perturbation, the mean density within the virial radius (at redshift z) in units of the global mean density (at redshift z) can be parameterized by

$$\bar{\rho}_v(\Omega_z, \Lambda_z) = 178\Omega_z^{-0.57}C(\Omega_z, \Lambda_z). \quad (7)$$

For $\Omega_z = 1$ and $\Lambda_z = 0$, it is well known that $\bar{\rho}_v = 178$, a result first derived by Gunn & Gott (1972). In equation (7) $C(\Omega_z, \Lambda_z)$ (a function of both Ω_z and Λ_z) has a value close to unity. It has been shown that $C = 1$ is a good approximation for both $\Lambda_z = 0$ model (e.g., Lacey & Cole 1993) and $\Lambda_z + \Omega_z = 1$ model (e.g., ECF) for the range of Ω_z of interest ($0.1 < \Omega_z < 1.0$). The mass within the comoving virial radius, r_v , at redshift z , is therefore

$$M_v(z) = \frac{4\pi}{3} r_v^3 \bar{\rho}_v(\Omega_z, \Lambda_z) \rho_c \Omega_0 \\ \approx 0.58 \times 10^{14} \Omega_z^{-0.57} \Omega_0 r_v^3 C(\Omega_z, \Lambda_z) \quad (8)$$

where ρ_c is the critical density at $z = 0$. Since the spherical perturbation smoothed by a Gaussian window of comoving radius r_f is, by assumption, just virialized at the redshift in question, we have another expression for M_v as a function of r_f :

$$M_v(z) = (2\pi)^{3/2} r_f^3 \rho_c \Omega_0 = 4.347 \times 10^{12} \Omega_0 r_f^3 \quad (9)$$

Next, we need to relate M_v to M_A , the latter of which is observationally more obtainable. We assume the following simple relationship:

$$M_A = M_v \left(\frac{r_A}{r_v} \right)^{3-\alpha}. \quad (10)$$

This relation holds exactly, if the density profile of the cluster has the power-law form:

$$\rho(r) \propto r^{-\alpha}. \quad (11)$$

But, in general, the density profile of a cluster does not have a power-law form, so $\alpha(\Omega_z, \Lambda_z, M_A, P_k)$ should only be considered as a fitting parameter, which should, in principle, be dependent on both the cluster mass and underlying cosmology. However, motivated by the insight of Navarro, Frenk, & White (1996) that there seems to be a universal function (as a function of scaled radius in units of the virial radius each individual halo) for density profiles of dark matter halos, independent of cosmology and halo mass, it is hoped that α will only be a *weak* function of both the underlying cosmology and cluster mass. As a matter of fact, as we will show below, the best fit to N-body results requires that α be a constant equal to 2.3, in harmony with the work of Navarro et al. (1996). Combining equations 8,9,10 yields

$$r_f = 3.617 r_A^{(\alpha-3)/\alpha} \left(\frac{M_A}{2.058 \times 10^{14}} \right)^{1/\alpha} \Omega_z^{0.19(\alpha-3)/\alpha} \Omega_0^{-1/\alpha} C(\Omega_z, \Lambda_z)^{(\alpha-3)/3\alpha}. \quad (12)$$

This equation allows us to determine the smoothing radius r_f for a cluster of mass M_A (within radius r_A), given α . We see that r_f will be completely deterministic, *if α and C can be specified a priori*. As we will subsequently show, we will choose to fix $C = 1$ and let its dependence on Ω_z and Λ_z be absorbed by another fitting parameter δ_c (see below). Therefore, the final equation for r_f that we will use is

$$r_f = 3.617 r_A^{(\alpha-3)/\alpha} \left(\frac{M_A}{2.058 \times 10^{14}} \right)^{1/\alpha} \Omega_z^{0.19(\alpha-3)/\alpha} \Omega_0^{-1/\alpha}. \quad (13)$$

In this equation α is the only adjustable parameter. But as will be shown later, α turns out to be a constant. Therefore, r_f is *no longer an adjustable parameter, rather it is a unique function of only M_A and r_A* . Another useful expression is to relate M_v to M_A (obtained by combining equations 9 and 13) in terms of r_A :

$$M_v = 2.058 \times 10^{14} r_A^{3(\alpha-3)/\alpha} \left(\frac{M_A}{2.058 \times 10^{14}} \right)^{3/\alpha} \Omega_z^{0.57(\alpha-3)/\alpha} \Omega_0^{(\alpha-3)/\alpha} \quad (14)$$

or

$$M_A = 2.058 \times 10^{14} r_A^{3-\alpha} \left(\frac{M_v}{2.058 \times 10^{14}} \right)^{\alpha/3} \Omega_z^{0.19(3-\alpha)} \Omega_0^{(3-\alpha)/3}. \quad (15)$$

We note that, in the special case where $r_A = r_v$, we have (from equation 9)

$$r_f = \left(\frac{M_A}{4.347 \times 10^{12}} \right)^{1/3} \Omega_0^{-1/3}, \quad (16)$$

which is independent of α , and the virial radius is

$$r_v = \left(\frac{M_A}{2.058 \times 10^{14}} \right)^{1/3} \Omega_z^{0.19} \Omega_0^{-1/3}. \quad (17)$$

The circular velocity of the (just virialized) halo at redshift z can be expressed as

$$v_c = \left[\frac{GM_v(1+z)}{r_v} \right]^{1/2} = 7.4 \times 10^2 \left(\frac{M_A}{1.0 \times 10^{14}} \right)^{1/3} \Omega_z^{-0.095} \Omega_0^{1/6} (1+z)^{1/2} \text{ km/s}. \quad (18)$$

Note that the dependences of v_c on Ω_z and Ω_0 are very weak. But v_c depends rather strongly on z and somewhat strongly on M_v . The 1-d velocity dispersion $\sigma_{||}$ is just equal to $v_c/\sqrt{2}$. Another useful relation is between r_f and v_c (or $\sigma_{||}$):

$$r_f = 3.845 \times 10^{-3} v_c \Omega_z^{0.095} \Omega_0^{-1/2} (1+z)^{-1/2}, \quad (19)$$

where v_c is in km/s.

Once we have uniquely determined the smoothing window for a given cluster mass and cosmology (equation 13), there is only one last parameter to be specified before the abundance of peaks forming clusters of a given mass is uniquely fixed: we need to specify the required peak height such that density peaks with such a height just collapse and virialize at the redshift in question. Here once again, we are guided by the spherical perturbation model, and use δ_c as a parameter to quantify the required peak height. δ_c is the linear overdensity of a peak at the concerned redshift at which a peak just collapses and virializes. δ_c is 1.68 in the spherical top-hat collapse in an $\Omega_z = 1$ model (Gunn & Gott 1972). Since realistic density perturbations are likely to be non-spherical and non-top-hat and there are models other than those with $\Omega_z = 1$ also being considered, δ_c can only be treated as a fitting parameter, to be determined by comparing to N-body simulations. In other words, the spherical collapse model is not applied explicitly, rather it is used as a guide for an initial guess of δ_c . The actual collapse, or some portion of the collapse in time or in space, of a density peak may not be spherical. For example, a triaxial proto-cluster will require a lower value of δ_c than a spherical proto-cluster (More, Heavens, & Peacock 1986). The validity of our method does not critically depend on the spherical collapse model, rather it is made valid by comparing to N-body simulations treating δ_c as a fitting parameter. Although δ_c could depend on P_k and cluster virial mass M_v as well as Ω_z and Λ_z , we will restrict our fitting procedure as if δ_c only depends on Ω_z and Λ_z . In any case, the final fit to N-body results proves that this assumption is good.

We now set down the basic formulae from BBKS for computing the number density of peaks of appropriate sizes and heights for a Gaussian density field. The differential peak density is

$$N_{pk}(\nu) = \frac{1}{(2\pi)^2 R_*^3} e^{-\nu^2/2} G(\gamma, \gamma\nu), \quad (20)$$

where $G(\gamma, w)$ is, for the convenience of calculation, an analytic formula approximating the exact three-dimensional integral (see equation A12 of BBKS). $G(\gamma, w)$ is accurate to better than 1% over the range $0.3 < \gamma < 0.7$ and

$-1 < w < \infty$ with the accuracy being better than 0.1% for $w > 1$, according to BBKS:

$$G(\gamma, w) = \frac{w^3 - 3\gamma^2 w + [B(\gamma)w^2 + C_1(\gamma)] \exp[-A(\gamma)w^2]}{1 + C_2(\gamma) \exp[-C_3(\gamma)w]} \quad (21)$$

(equation 4.4 of BBKS), where $w \equiv \gamma\nu$. For all the models which we have computed or are of current interest we have $\gamma > 0.7$ and $w > 1.1$ in most cases with the lowest values being $\gamma = 0.58$ and $w = 0.84$. Therefore, it is accurate to use $G(\gamma, w)$ for models of current interest. The various symbols are defined as follows.

$$\begin{aligned} A &= \frac{5/2}{9 - 5\gamma^2} \\ B &= \frac{432}{(10\pi)^{1/2}(9 - 5\gamma^2)^{5/2}} \\ C_1 &= 1.84 + 1.13(1 - \gamma^2)^{5.72} \\ C_2 &= 8.91 + 1.27 \exp(6.51\gamma^2) \\ C_3 &= 2.58 \exp(1.05\gamma^2) \end{aligned} \quad (22)$$

(equation 4.5 of BBKS). The parameters γ and R_* are related to the moments of the power spectrum:

$$\begin{aligned} \gamma &\equiv \frac{\sigma_1^2}{\sigma_2\sigma_0} \\ R_* &\equiv \sqrt{3} \frac{\sigma_1}{\sigma_2} \end{aligned} \quad (23)$$

(equation 4.6a of BBKS), and σ_j are spectral moments:

$$\sigma_j \equiv \int \frac{k^2 dk}{2\pi^2} P_k k^{2j} W^2(kr_f) \quad (24)$$

(equation 4.6c of BBKS). We are now ready to derive the cluster mass function by counting peaks of appropriate sizes and heights. The procedure can be described in four steps:

1. For a cluster mass M_A , we find r_f using equation 13.
2. We smooth the power spectrum P_k by the square of a Gaussian window of radius r_f (equation 6) and then compute σ_0 , γ and R_* (equations 23,24).
3. Requiring that $\nu\sigma_0 = \delta_c$ yields the threshold peak height $\nu_t = \delta_c/\sigma_0$.
4. Integrating equation 20 from ν_t to ∞ gives the cumulative cluster mass function:

$$n(> M_A) = \int_{\nu_t}^{\infty} N_{pk}(\nu) d\nu. \quad (25)$$

To summarize, we have three adjustable parameters: $\alpha(\Omega_z, \Lambda_z, M_A, P_k)$, $\delta_c(\Omega_z, \Lambda_z)$ and $C(\Omega_z, \Lambda_z)$. In general, $\alpha(\Omega_z, \Lambda_z, M_A, P_k)$ should be a function of four variables, Ω_z , Λ_z , M_A and P_k , whereas δ_c and C should depend only on Ω_z and Λ_z . We choose to fix $C(\Omega_z, \Lambda_z)$ to be unity, independent of cosmological parameters, and treat only α and δ_c as two adjustable parameters. Since both parameters (C and δ_c) depend on the same cosmological parameters, this treatment is justified and simplifies the fitting procedure; the dependence of $C(\Omega_z, \Lambda_z)$ on cosmological parameters is assumed to be absorbed by $\delta_c(\Omega_z, \Lambda_z)$.

We now turn to N-body simulations to calibrate GPM to compute the cluster mass function, i.e., to determine the two fitting parameters in GPM, α and δ_c . We have thirty two cosmological models at our disposal to calibrate GPM and test its accuracy. The models are listed in Table 1. The second and third columns are the density parameter and cosmological constant of the model, respectively. The fourth column is the linear rms density fluctuation in an $8 h^{-1}\text{Mpc}$ top-hat sphere at $z = 0$. The fifth column, EP (Excess Power), is a parameter to describe the shape of the power spectrum on scales $\sim 8 - 300 h^{-1}\text{Mpc}$, introduced by Wright et al. (1992). The definition is $EP \equiv 3.4\sigma_{25}/\sigma_8$, where σ_{25} is the linear rms density fluctuation in a $25 h^{-1}\text{Mpc}$ top-hat sphere at $z = 0$. The last column indicates the type of power spectrum used (details are given in the table footnotes).

Some models are physically self-consistent in the sense that their power spectrum transfer functions are computed for the given cosmological parameters, while others are not. The latter are included to increase the coverage of the parameter space for calibration purposes. Taken together these thirty two models span the ranges of Ω_z , Λ_z , σ_8 and EP of current interest: $\Omega_z = 0.2 \rightarrow 1.0$, $\Lambda_z = 0.0 \rightarrow 0.8$, $\sigma_8 = 0.35 \rightarrow 1.5$, and $EP = 0.735 \rightarrow 1.923$. As a note, Wright et al. (1992) find that the range of EP that fits the COBE data is $1.30 \pm 0.15 (1\sigma)$, which is consistent with analysis of the galaxy power spectrum by Peacock & Dodds (1994) and Feldman, Kaiser & Peacock (1994), or observations of large-scale galaxy clustering by Maddox et al. (1990). The reason that we use EP rather than Γ ($= \Omega_0 h$) is that Γ can only be used for CDM type models with $n = 1$.

Each model is run using a particle-mesh code with a box size $400 h^{-1}\text{Mpc}$. A large simulation box is needed in order to produce a significant number of the rich but rare clusters. The simulation box contains 720^3 cells and $240^3 = 10^{7.1}$ dark matter particles, with a particle mass of $1.3 \times 10^{12} \Omega_0 h^{-1} M_\odot$. The mass resolution seems adequate for our purpose: a cluster of mass $6 \times 10^{14} h^{-1} M_\odot$ contains $462 \Omega_0^{-1}$ particles. In each simulation, clusters are selected as the maxima of the mass distribution within spheres of comoving radius of $r_A = 1.5 h^{-1} \text{Mpc}$. The mass of each cluster is determined in a sphere within the Abell radius r_A . The results are not sensitive to the cluster-finding algorithm *as long as the mass is defined within a chosen radius*. In other words, different group-finding algorithms such as friends-of-friends or DENMAX are all able to locate the density peaks properly.

Before we present our numerical results, it is important to check resolution effect. We make the following resolution calibration test. We run two simulations for the SCDM model (model 1 in Table 1) with an identical initial realization in a box of size $L = 128 h^{-1}\text{Mpc}$. One of the two simulations uses the same PM code as for the thirty two models listed in Table 1 and has the same numerical resolution ($1.39 h^{-1}\text{Mpc}$); the other simulation has a much higher resolution ($0.0625 h^{-1}\text{Mpc}$) based on the P³M scheme utilizing a special computer chip (GRAPE) to solve the PP part of the force computation (Briau, Summers & Ostriker 1995). Since the resolution element of the P³M simulation is much smaller than the Abell radius, it can be considered as having an infinite resolution

TABLE 1
LIST OF PARAMETERS FOR 32 MODELS

Model	Ω_0	Λ_0	σ_8	$EP \equiv 3.4\sigma_{25}/\sigma_8$	Comment
1	1.000	0.000	1.050	0.956	SCDM ^a
2	1.000	0.000	0.700	0.956	SCDM ^a
3	1.000	0.000	0.525	0.956	SCDM ^a
4	1.000	0.000	0.350	0.956	SCDM ^a
5	1.000	0.000	1.050	1.088	$P_k = k^{-1}$
6	1.000	0.000	0.808	1.088	$P_k = k^{-1}$
7	1.000	0.000	0.700	1.088	$P_k = k^{-1}$
8	1.000	0.000	0.525	1.088	$P_k = k^{-1}$
9	1.000	0.000	0.350	1.088	$P_k = k^{-1}$
10	1.000	0.000	1.050	1.923	$P_k = k^{-2}$
11	1.000	0.000	0.808	1.923	$P_k = k^{-2}$
12	1.000	0.000	0.700	1.923	$P_k = k^{-2}$
13	1.000	0.000	0.525	1.923	$P_k = k^{-2}$
14	0.350	0.000	0.800	1.196	OCDM1 ^b
15	0.410	0.000	0.689	1.196	OCDM1 ^b
16	0.446	0.000	0.632	1.196	OCDM1 ^b
17	0.520	0.000	0.524	1.196	OCDM1 ^b
18	0.600	0.000	1.000	1.060	OCDM2 ^b
19	0.661	0.000	0.818	1.060	OCDM2 ^b
20	0.692	0.000	0.730	1.060	OCDM2 ^c
21	0.750	0.000	0.575	1.060	OCDM2 ^c
22	0.818	0.000	0.404	1.060	OCDM2 ^c
23	0.400	0.600	0.790	1.225	LCDM1 ^d
24	0.692	0.308	0.591	1.225	LCDM1 ^d
25	0.842	0.158	0.460	1.225	LCDM1 ^d
26	0.200	0.800	1.500	1.225	LCDM2 ^e
27	0.355	0.645	1.321	1.225	LCDM2 ^e
28	0.458	0.542	1.211	1.225	LCDM2 ^e
29	0.573	0.427	1.088	1.225	LCDM2 ^e
30	0.667	0.333	0.982	1.225	LCDM2 ^e
31	0.796	0.204	0.813	1.225	LCDM2 ^e
32	0.871	0.129	0.690	1.225	LCDM2 ^e

^athe standard CDM model with Hubble constant $H_o = 50\text{km/s/Mpc}$, $\Omega_0 = 1.0$ and $n = 1.0$, where n is the power index at very large scale. BBKS power spectrum transfer function (equation G3) is used

^ban open CDM model with Hubble constant $H_o = 70\text{km/s/Mpc}$, $\Omega_0 = 0.35$ and $n = 1.0$; BBKS power spectrum transfer function (equation G3) is used.

^can open CDM model with Hubble constant $H_o = 60\text{km/s/Mpc}$, $\Omega_0 = 0.60$ and $n = 1.0$; BBKS power spectrum transfer function (equation G3) is used.

^da CDM model with a cosmological constant with Hubble constant $H_o = 65\text{km/s/Mpc}$, $\Omega_0 = 0.40$, $\Lambda_0 = 0.60$ and $n = 0.95$; the power spectrum transfer function is computed as in Cen et al. 1993.

^ea CDM model with a cosmological constant with Hubble constant $H_o = 100\text{km/s/Mpc}$, $\Omega_0 = 0.20$, $\Lambda_0 = 0.80$ and $n = 0.95$; the same power spectrum as LCDM1 is used.

Figure 1

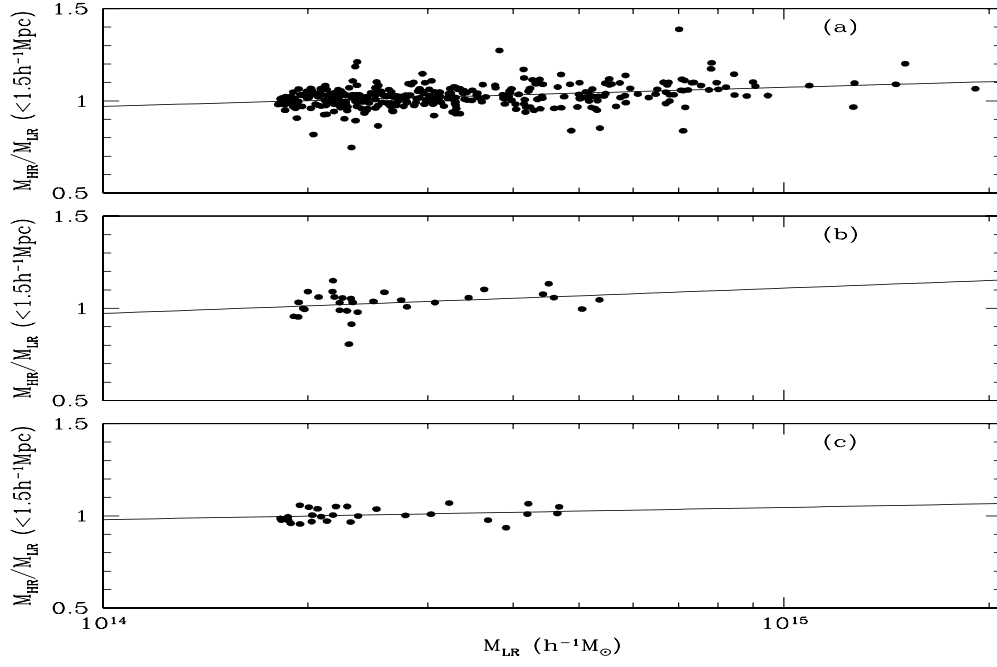
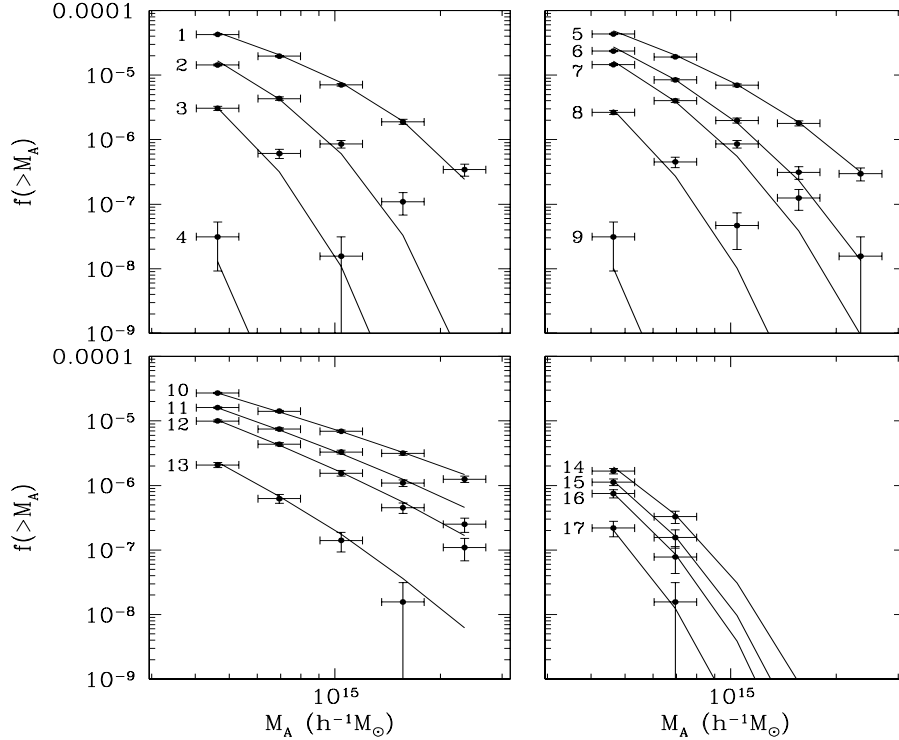


FIG. 1.— M_{HR}/M_{LR} is plotted against M_{LR} for the three models. The solid line in each plot is the best linear fit: $M_{HR}/M_{LR} = a + b \log_{10} M_{LR}$, where M_{LR} is in $h^{-1} M_{\odot}$. We find (a,b) to be $(-0.469, 0.103)$, $(-0.0528, 0.0662)$, $(-0.952, 0.137)$ for models (1,14,29), respectively.

Figure 2a



(2a)

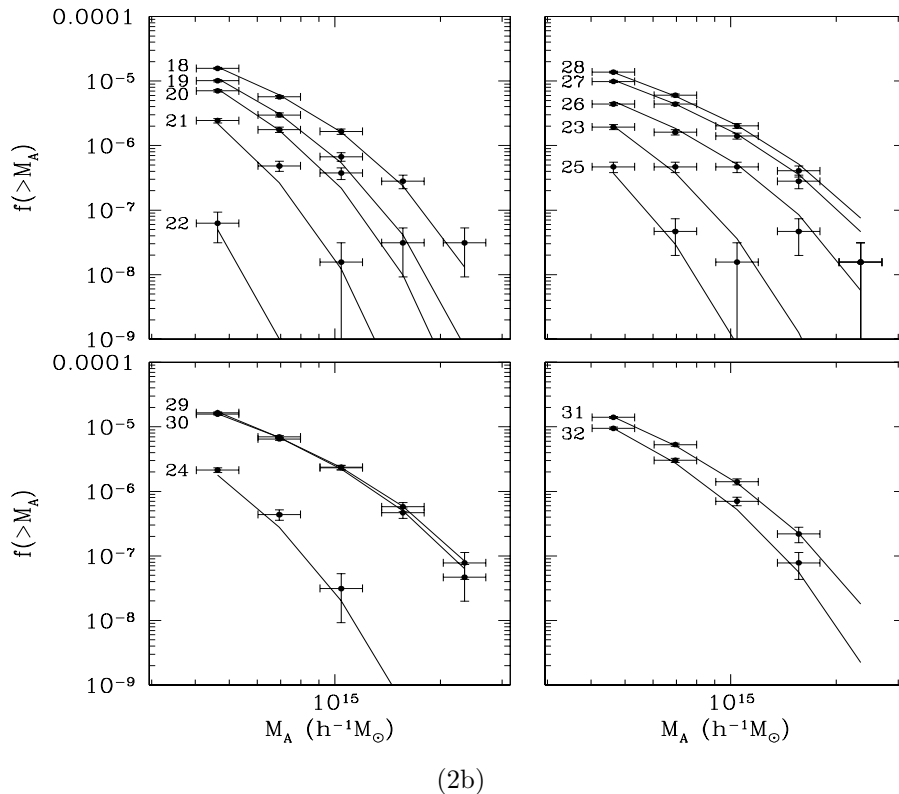


Figure 2b

FIG. 2.— Mass functions of various models. Each curve is labeled by its model number from Table 1. The simulation results are shown as symbols with horizontal errorbars being the uncertainties in the mass determination (15%) and the vertical errorbars being the statistical 1σ errorbars for the number of clusters. The solid curves in Figure 2 are the results from GPM. Note that simulation box size limits the density of clusters to $> 1.56 \times 10^{-8} h^3 \text{Mpc}^{-3}$, when there is only one cluster in the whole box. At $f(> M_A) = 10^{-6} h^3 \text{Mpc}^{-3}$, there are 65 clusters in the simulation box.

(i.e., representing the truth) for the purpose of calibrating our low resolution results. Because the two simulations have identical initial conditions, we are able to identify every rich cluster in one simulation with its counterpart in the other. Having made such a one-to-one correspondence we can compute the ratio M_{HR}/M_{LR} (HR stands for high resolution and LR for low resolution) as a function of cluster mass M_{LR} . This allows us to make corrections to M_{LR} in the lower resolution simulation. The above resolution calibration procedure is repeated for an open CDM model (model 14 in Table 1) and a CDM model with a cosmological constant (model 23 in Table 1).

Figures (1a,b,c) show the results for the three models, where M_{HR}/M_{LR} is plotted against M_{LR} . The solid line in each plot is the best linear fit: $M_{HR}/M_{LR} = a + b \log_{10} M_{LR}$, where M_{LR} is in $h^{-1} M_{\odot}$. We find (a, b) to be $(-0.469, 0.103)$, $(-0.0528, 0.0662)$, $(-0.952, 0.137)$ for models (1,14,23), respectively. Let us call the three fitting functions (M_{HR}/M_{LR}) as $R_1(M)$, $R_{035}(M)$, $R_{04}(M)$, for the three models run: $\Omega_z = 1$ (model 1 in Table 1), $\Omega_z = 0.35$ and $\Lambda_z = 0$ (model 14), and $\Omega_z = 0.40$ and $\Lambda_z = 0.60$ (model 23). Then, for the mass of each cluster, M_{LR} , we correct it by multiplying it by $R_1 + (R_{035} - R_1)(1 - \Omega_z)/0.65$ in an open model, or by $R_1 + (R_{04} - R_1)(1 - \Omega_z)/0.60$ in a Λ model, where Ω_z is the density parameter of the model under consideration. From Figure 1 we see that the typical correction is about 5-10% in the upward direction with a dispersion of $\sim 5\%$; i.e., lower resolution simulations slightly underestimate the mass within the Abell radius, as expected. Calibrating the lower resolution simulation results we assign an errorbar of 15% for each cluster mass.

We are now ready to find the best fitting parameters (α, δ_c) by comparing results from GPM to the direct N-body results. Before starting the fitting procedure, we have some rough idea about what the values of α and δ_c may be. We pick $\alpha = 2.5$ and $\delta_c = 1.5$ as an initial guess. In the end, the best values are found to be

$$\alpha = 2.3, \quad (26)$$

a constant independent of the cluster mass and cosmology, and

$$\delta_c = \begin{cases} 1.40 - 0.01(1.0 - \Omega_z) & \text{for } \Lambda_z = 0 \\ 1.40 + 0.10(1.0 - \Omega_z) & \text{for } \Omega_z + \Lambda_z = 1. \end{cases} \quad (27)$$

The best overall fit for all the models is judged by the author by direct visual examination. We find it very difficult to design an automated fitting procedure to be gauged by some objective parameters, because of the enormous range of the number densities of clusters and hard-to-define errorbars hence weighting schemes for the densities. But as we will see, the final fits are probably as good as one would have hoped, which suggests that our somewhat subjective fitting procedure works very well. In any case, the final fit values span very narrow ranges (in fact, α turns out to be a constant, and δ_c varies from 1.40 to 1.39 from $\Omega_z = 1$ to 0 in $\Lambda_z = 0$ models, from 1.40 to 1.36 from $\Omega_z = 1$ to 0 in $\Lambda_z + \Lambda_z = 1$ models), which indicates that the fitting procedure is robust and stable. We note that the fitted value of α is in excellent agreement with observations (Carlberg et al. 1996; Fischer et al. 1997). It seems useful to estimate the uncertainties in the fitted values of α and δ_c .

However, the sensitivity of a fit to the two parameters depends on the fitted mass function itself: a low amplitude mass function depends more sensitively on the two parameters than a high amplitude mass function. This is so, of course, because the abundance of rarer objects depends more sensitively on the parameters. Roughly speaking, α serves more to fix the shape of the mass function in a somewhat less sensitive way, while δ_c determines the overall amplitude and more sensitively the amplitude on the high mass end of the mass function. Our estimates on the uncertainties are $\Delta\alpha = 0.1$ and $\Delta\delta_c = 0.01$.

Figures (2a,b) show the simulation results as symbols for 32 models with horizontal errorbars being the uncertainties in the mass determination (15%) and the vertical errorbars being the statistical 1σ errorbars. Note that simulation box size limits the density of clusters to $> 1.56 \times 10^{-8} h^3 \text{Mpc}^{-3}$, when there is only one cluster in the whole box. At $f(> M_A) = 10^{-6} h^3 \text{Mpc}^{-3}$, there are 65 clusters. The solid curves in Figure 2 are the results from GPM. We see that the GPM results fit remarkably well the simulation results for all the thirty two models examined. We note that the actual errorbars should be larger than what are shown for the simulated results because of cosmic variances; i.e., the simulation boxsize, although quite large being $400 h^{-1} \text{Mpc}$, may still not be large enough to have the cosmic variance diminished, especially for models with significant power on several hundred megaparsecs scales. In any case, the GPM results fit the N-body results for all the models within 2σ in the vertical axis, and within a factor of 1.25 in the horizontal axis. Since the observed mass function (BC) has uncertainties in mass about a factor 2.0 and in number density about a factor ≥ 2.0 , the GPM results are practically precise, for the purpose of comparing model results computed using GPM with observations.

At this point it seems appropriate to reiterate the virtue of the current method. The essential unique ingredients are the introduction of two adjustable parameters, α and δ_c , the first of which turns out to be a constant and the second of which can be simply expressed as a function of Ω_z (the density parameter at the redshift in question). Note that the fitted parameter $\delta_c(\Omega_z)$ has a slightly different form for the case with $\Lambda_z = 0$ than for the case with $\Omega_z + \Lambda_z = 1$. The fact that δ_c is only a rather weak function of Ω_z in both cases indicates that the method is robust.

2.2. Gaussian Peak Method for Cluster Correlation Function

Having found that the initial density peaks, appropriately defined, indeed correspond to the clusters formed at late times, as indicated by the goodness of the fits of the results from GPM to the N-body results in terms of cluster mass function presented in the preceding section, we have some confidence that we may be able to compute the cluster-cluster two-point correlation function using GPM. We will now proceed along this route.

Even in the linear regime where dynamic contribution to the clustering can be ignored, the primary difficulty in calculating the cluster-cluster two-point correlation function using Gaussian peaks is the ambiguity of relating appropriate peaks to the clusters of interest. This ambiguity is reflected in one's inability to fix the smoothing length r_f and the threshold peak height ν_t . The GPM, described

in §2, eliminates this ambiguity by simultaneously fixing both r_f and ν_t . This is achieved by demanding that the appropriate peaks yield the correct cluster mass function, when compared to direct N-body simulations.

Following BBKS, we use the following approximate formula, which is applicable when the correlation function is smaller than unity [however, BBKS state that it may well be a reasonable approximation even when the statistical correlation function (first term at the right hand side of equation 28, see below) is not really small], to compute the final cluster-cluster correlation function including linear dynamical contributions:

$$\xi_{pk,pk} \approx \left(\frac{\langle \tilde{\nu} \rangle}{\sigma_0} + 1 \right)^2 \xi_{\rho,\rho}, \quad (28)$$

(equation 6.63 of BBKS), where $\xi_{\rho,\rho}$ is the two-point density auto-correlation function, and $\langle \tilde{\nu} \rangle$ is defined by

$$\tilde{\nu} \equiv \int_{\nu_t}^{\infty} [\nu - \gamma\theta/(1 - \gamma^2)] N_{pk} d\nu \quad (29)$$

(equation 6.45 of BBKS), where ν_t is determined in the procedure described in §2; γ is defined in equation 23; N_{pk} is defined in equation 20. Note that we have chosen a step function for threshold function $t(\nu/\nu_t)$ in equation 6.45 of BBKS to arrive at equation 29, i.e., only peaks above ν_t are assumed to be able to collapse and no peaks below ν_t are allowed to collapse. A smoother threshold function (e.g., Kaiser & Davis 1985; BBKS) may be used, but the primary effect will be to slightly change the fitting parameter δ_c . We therefore will use the sharp step function as the threshold function without loss of generality. θ is defined by

$$\theta \equiv \frac{3(1 - \gamma^2) + (1.216 - 0.9\gamma^4) \exp[-\gamma/2(\gamma\nu/2)^2]}{[3(1 - \gamma^2) + 0.45 + (\gamma\nu/2)^2]^{1/2} + \gamma\nu/2} \quad (30)$$

(equation 6.14 of BBKS). We note that equation 28 is valid in the linear regime when $\xi_{\rho,\rho}$ is much less than unity and it is not yet clear whether the approximation, coupled with our definitive peak identification method, also works in the mild nonlinear regime. Our goal is to find an approximation based on equation 28 which will give sufficiently accurate results for $\xi_{pk,pk}$ in the regime whose values are of order unity and below. For this reason we choose to modify equation 28 in the following manner: $\xi_{pk,pk} \approx \left(\frac{\langle \tilde{\nu} \rangle}{\sigma_0} + 1 \right)^2 \xi_{\rho,\rho} D(\bar{\xi}_{\rho,\rho})$, where $D(\bar{\xi}_{\rho,\rho})$ is a fitting parameter that depends only on $\bar{\xi}_{\rho,\rho}$, which is the mean two-point matter correlation function, defined as $\bar{\xi}_{\rho,\rho}(x) \equiv \frac{3}{x^3} \int_0^x \xi_{\rho,\rho}(y) y^2 dy$. The reason for using $\bar{\xi}_{\rho,\rho}$ instead of $\xi_{\rho,\rho}$ is that $\bar{\xi}_{\rho,\rho}$ is a better indicator of nonlinearity than $\xi_{\rho,\rho}$. The form of D should be constrained at the linear end: $D(0) = 1$. As we will show below, it turns out that equation 28 fits results very well; i.e., fitting to numerical results indicates that $D = 1$ is a good approximation for the interested range in $\xi_{pk,pk}$. To be clear, we use equation 28 for all the subsequent calculations of cluster correlation functions.

We now compare the two-point peak-peak correlation function, calculated using GPM described above, to the cluster-cluster two-point correlation function obtained

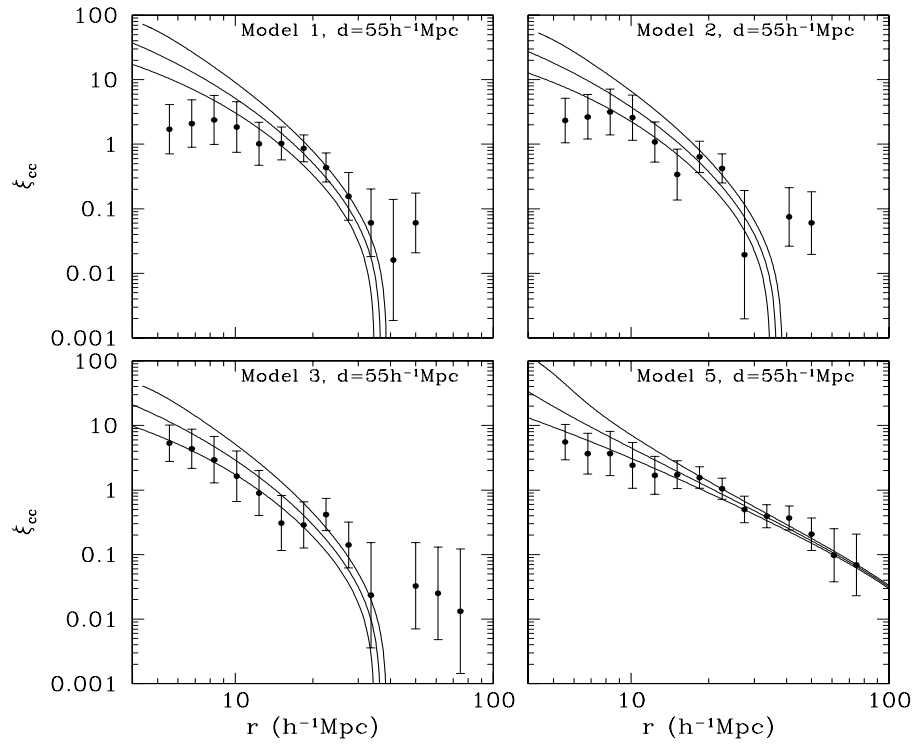


Figure 3a

(3a)

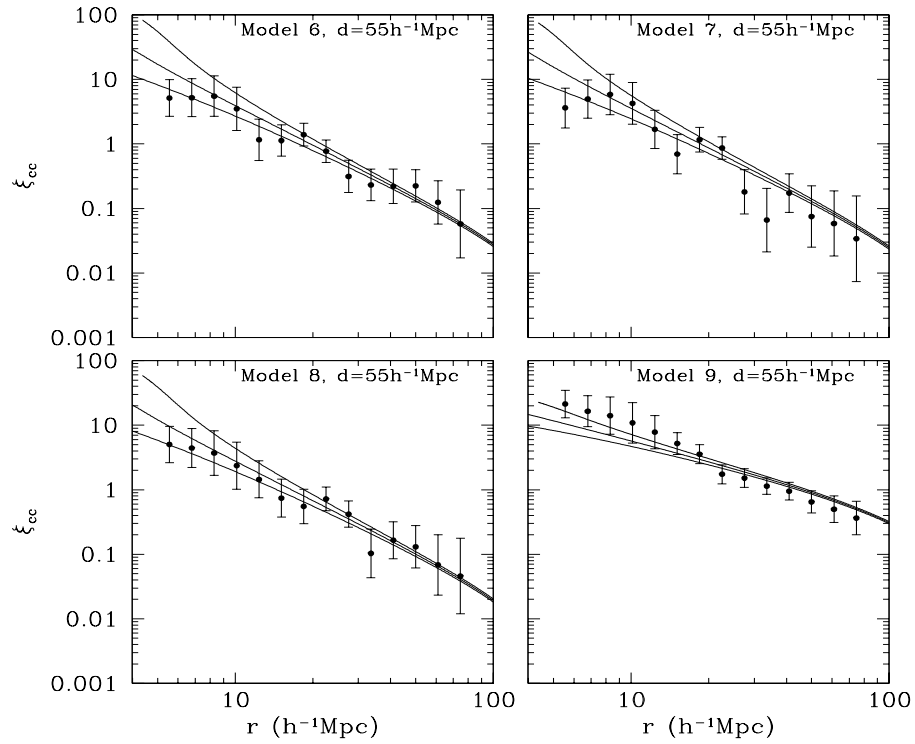


Figure 3b

(3b)

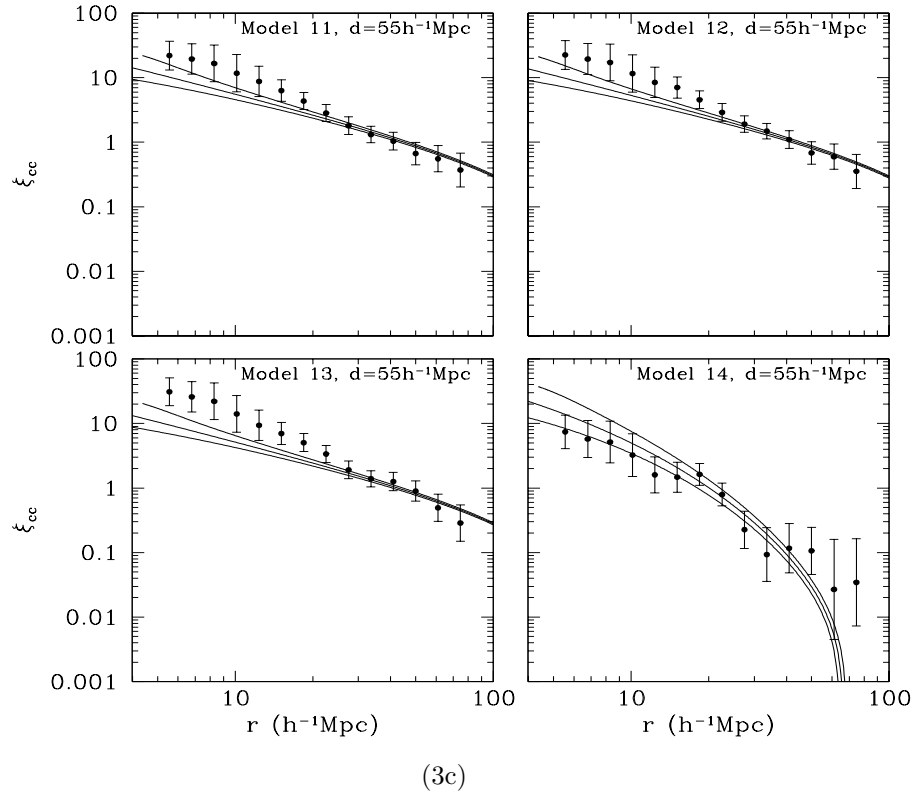


Figure 3c

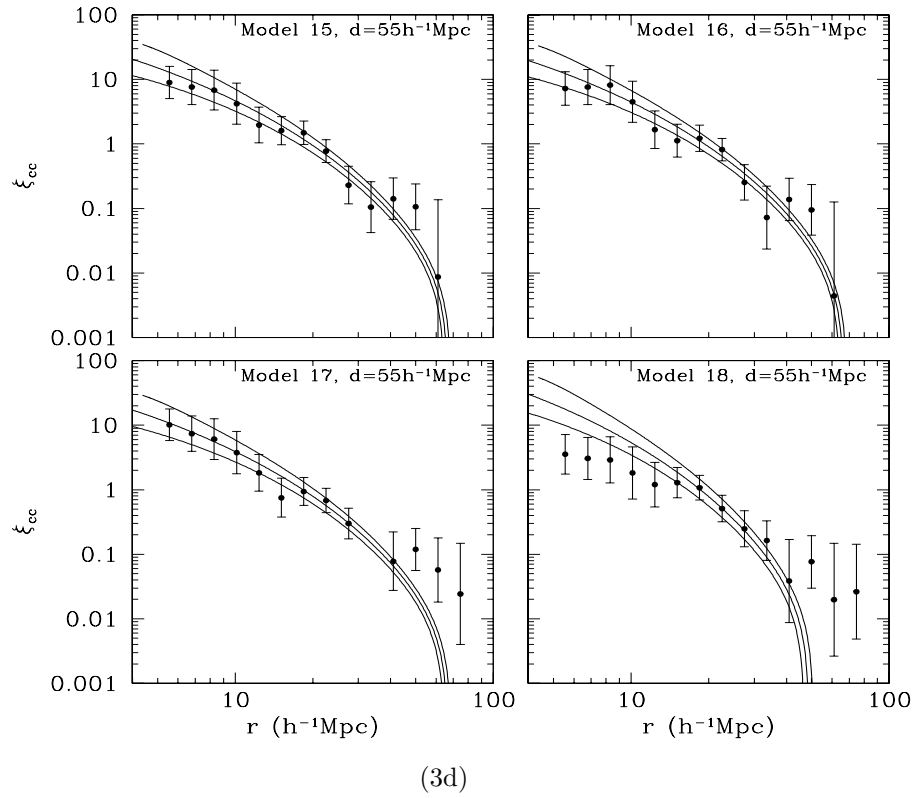


Figure 3d

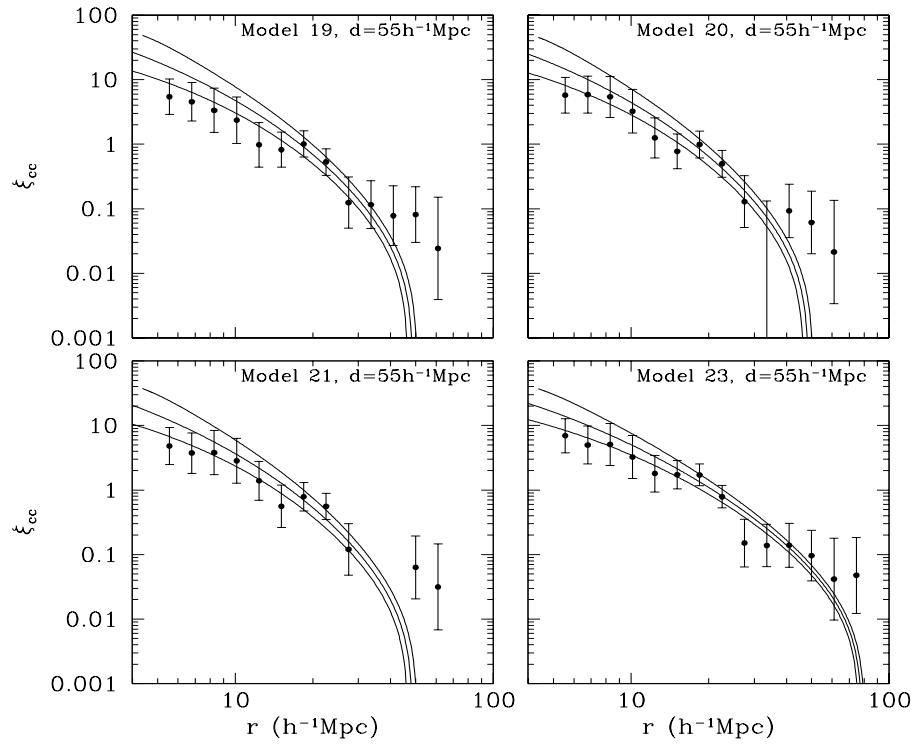


Figure 3e

(3e)

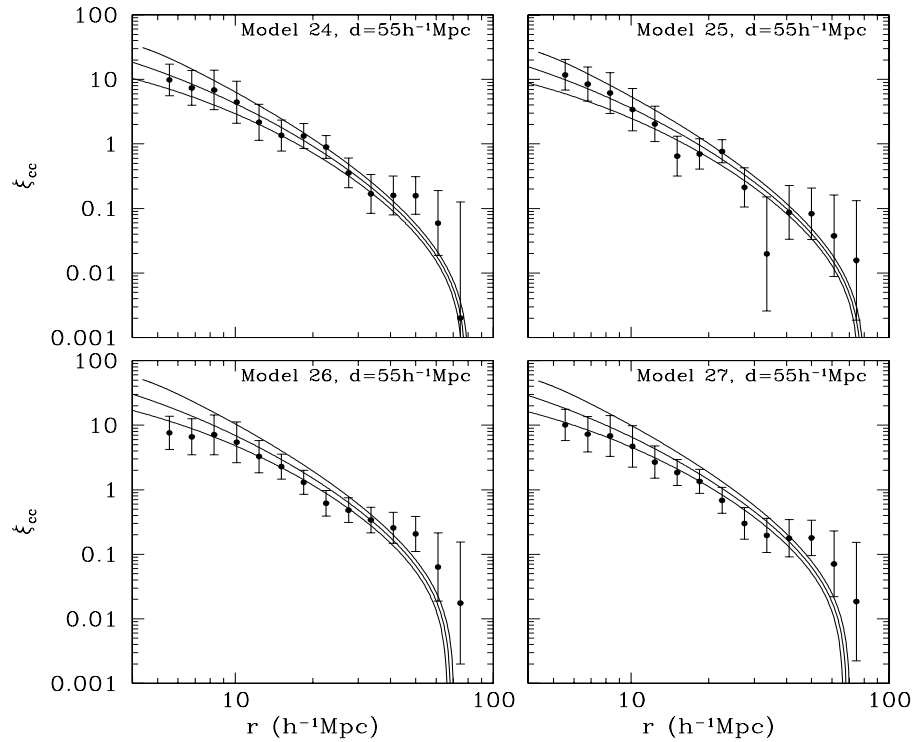


Figure 3f

(3f)

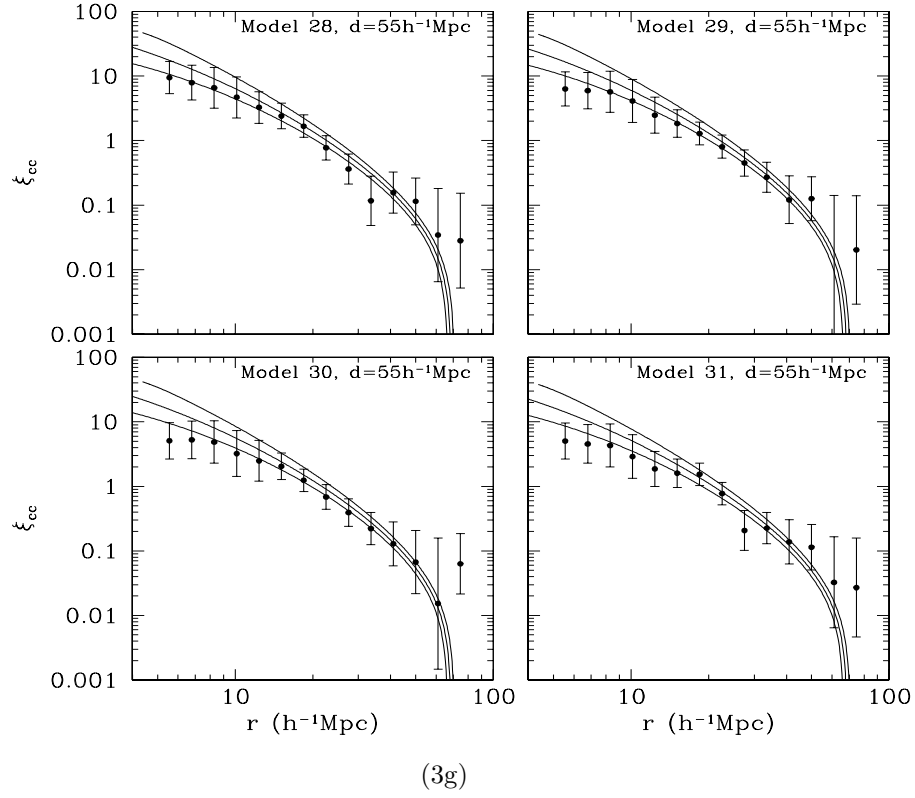


Figure 3g

FIG. 3.— The cluster correlation functions for clusters with mean separation of $55h^{-1}\text{Mpc}$, for 28 models as indicated in the panels. The errorbars are 1σ statistical. Three curves are shown in each panel for each model; the middle curve is obtained using equation 28 and the top and bottom curves are obtained by adding $\pm 2h^{-1}\text{Mpc}$ to each point of the middle curve in the x-axis.

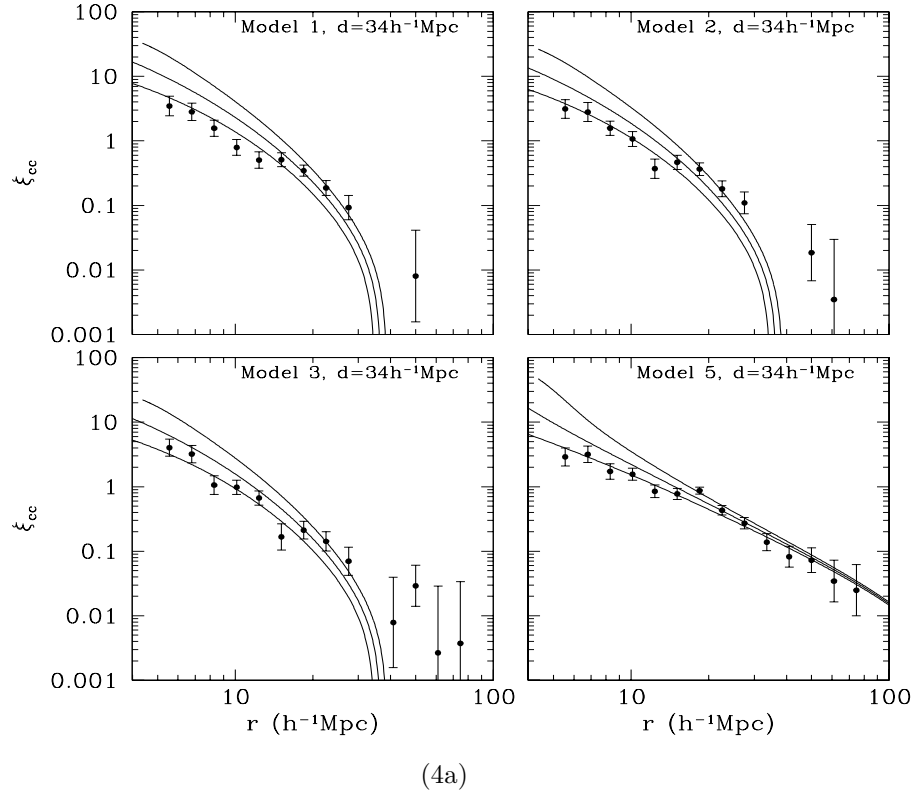


Figure 4a

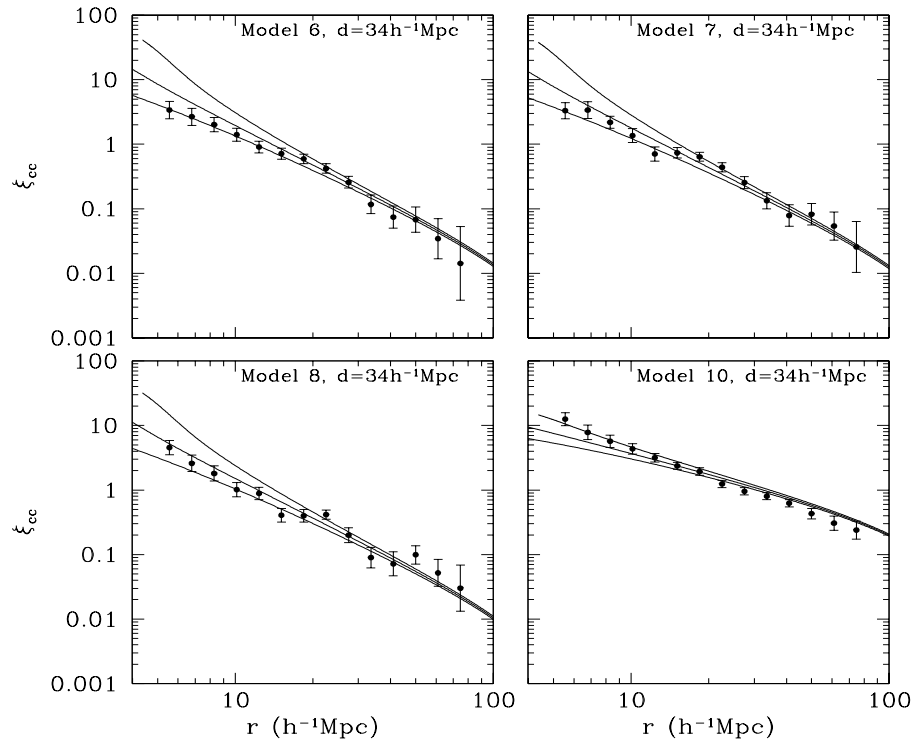


Figure 4b

(4b)

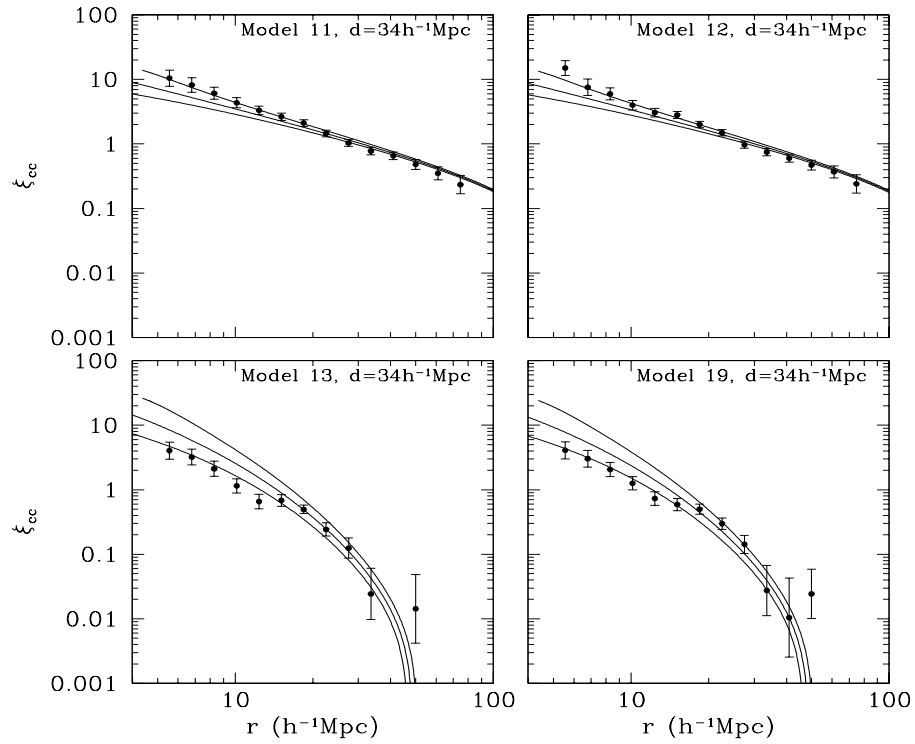


Figure 4c

(4c)

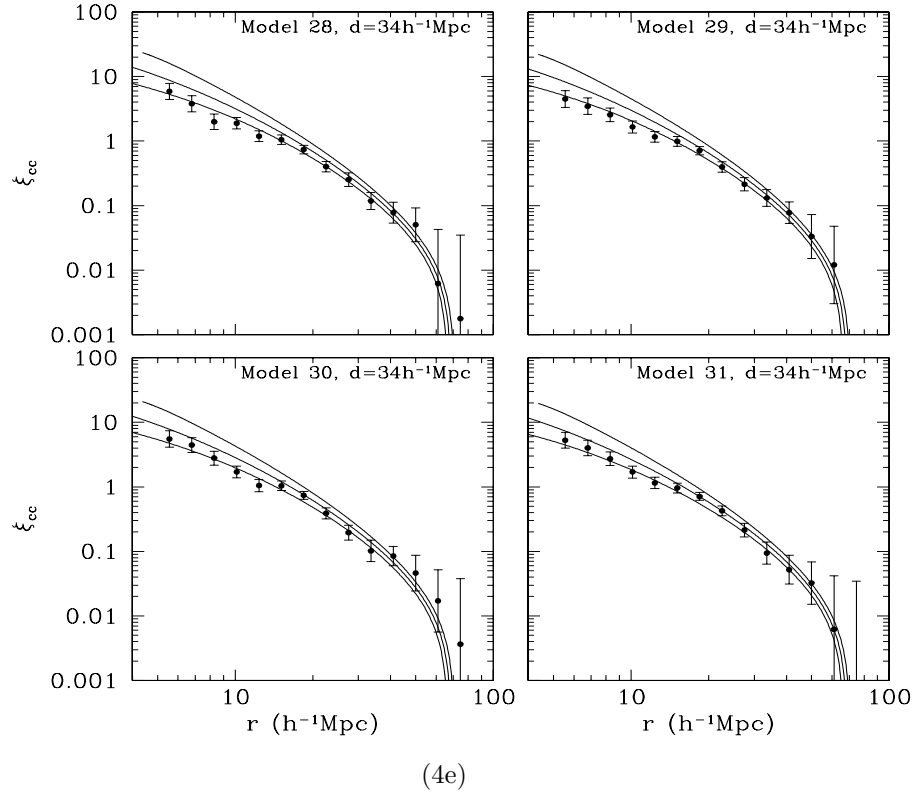
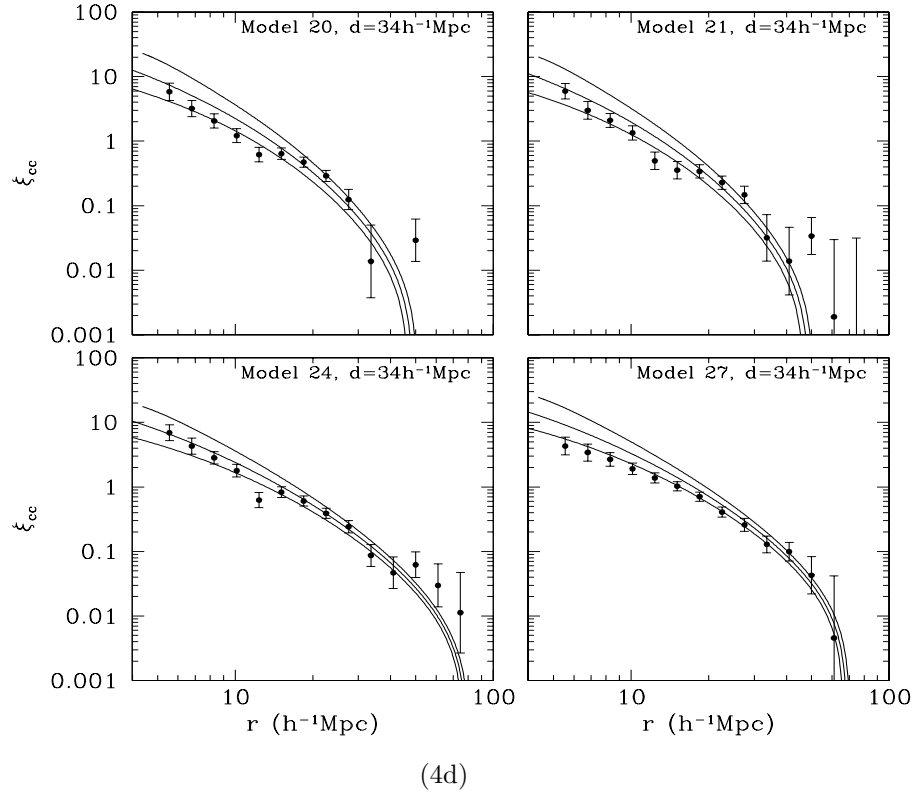


Figure 4d

Figure 4e

FIG. 4.— The cluster correlation functions for clusters with mean separation of $34h^{-1}\text{Mpc}$, for 20 models as indicated in the panels. The errorbars are 1σ statistical.

from N-body simulations. We compute the two-point correlation function from N-body simulations using the following estimator:

$$\xi_{cc}(r) = \frac{N_{CR}(r)}{N_{RR}(r)} - 1, \quad (31)$$

where $N_{CR}(r)$ and $N_{RR}(r)$ are the number of pairs between clusters and random spatial points and the number of pairs among random spatial points, respectively, at separation $r \rightarrow r + \Delta r$. The number of random spatial points for each realization within the simulation box ($400h^{-1}\text{Mpc}$) is chosen to be the same as the number of clusters in question. A total of 100 random realizations are made. The final ξ_{cc} is averaged over the 100 estimations and errorbars are estimated by separately computing the correlations for each of the eight octants of each simulation box.

Figures (3a,b,c,d,e,f,g) show the results of 28 models for clusters with mean separation of $55h^{-1}\text{Mpc}$. Three of the remaining four models do not have enough clusters whose masses exceed $1.4 \times 10^{14}h^{-1}M_{\odot}$ (the low mass cutoff for clusters found in the simulations). Model 32 is not shown only to save space, although the goodness of the fit of GPM result to the N-body result in Model 32 is comparable to that of Model 15 (top left panel of Figure 3d). Figures (4a,b,c,d,e) show the results of 20 models for clusters with mean separation of $34h^{-1}\text{Mpc}$. The models which are not shown, again, do not have enough clusters with masses greater than $1.4 \times 10^{14}h^{-1}M_{\odot}$, except for Model 32. The errorbars are 1σ statistical. Three curves are shown in each panel for each model; the middle curve is what is obtained using equation 28 and the top and bottom curves are obtained by adding $\pm 2h^{-1}\text{Mpc}$ to each point of the middle curve in the x-axis. We see that GPM works well in the range of scales where $\xi_{cc} = 0.1 - 2.0$ for all the models. Some models fit for even larger ranges. In particular, the correlation length seems quite accurately computable by GPM; $r_0(GPM) \pm 2h^{-1}\text{Mpc}$ [where $r_0(GPM)$ is the length scale where the correlation computed by GPM (equation 28) is unity] appears in agreement with the correlation length computed from direct N-body simulations for all the models studied here.

Several authors have used peaks in Gaussian density fields to compute the cluster-cluster two-point correlation function. Mann, Heavens, & Peacock (1993) use a method developed by Bond & Couchman (1988) which combines the Gaussian peak formalism with Zel'dovich approximation. Their method is analytically tractable and fast. Unfortunately, the accuracy of their method has not been carefully checked by N-body simulations and the two parameters r_f and δ_c (or r_f and ν_t) are not fully deterministic. It will be useful to apply the treatment of r_f , α and δ_c here to their method. Holtzman & Primack (1993) use a similar but somewhat different formula (Bardeen, Bond, & Efstathiou 1987) than what is used here to compute the cluster correlation function in some variants of CDM models. Aside from the slightly different formula used to compute the statistical and dynamical correlation terms, the primary difference between ours and theirs lies in the treatment of r_f and δ_c . In their work r_f is determined by the mass of a cluster in a rough way without taking into account the fact that the virial radius of a collapsed object

is different from the radius within which observed mass is defined, which consequently also affects δ_c . It might be beneficial to check their analytic method against N-body simulations for a wide range of models, before firm conclusions from detailed comparisons between models and observations can be drawn. Croft & Efstathiou (1994) have checked the same formula as used here to compute the correlation function of clusters using N-body simulations. The difference between our method and theirs is that r_f and δ_c in their approach are only roughly guessed based on a consideration of the approximate mass of clusters which determines r_f and the spherical collapse model which determines $\delta_c = 1.69$. Their Gaussian peak method agrees well with their N-body results for the poorer clusters ($d_c = 15h^{-1}\text{Mpc}$) in all three models ($\Omega_0 = 1$ model, $\Omega_0 = 0.2$ and $\Lambda_0 = 0.8$ model, and $\Omega_0 = 0.2$ and Λ_0 model) but the correlation functions from their Gaussian method are significantly lower than those from N-body simulations for richer clusters ($d_c = 35, 50h^{-1}\text{Mpc}$). The behavior of their results can be explained by the fact that they choose r_f to be independent of M_A (or d_c , the mean separation of clusters under consideration; a larger d_c corresponds to richer, more massive clusters), whereas in our case r_f correlates with M_A . Consequently, the correlations of richer clusters from the Gaussian method of Croft & Efstathiou (1994) are underestimated. The primary drawback of all these previous studies is the inability to uniquely identify a set of peaks with a set of clusters of interest. Again, this traces to the ambiguity of choosing r_f and ν_t . Our method eliminates this ambiguity entirely and the results seem satisfactory.

2.3. Calibrating Press-Schechter Formalism

We have shown in §2.1 and §2.2 that GPM works quite well for computing both the cluster mass and correlation functions. It is tempting to try the same arguments on the widely used Press-Schechter (1974; PS) formalism. We recall that the essential ingredient in GPM is the introduction of two parameters: α and δ_c . Fitting results from GPM to N-body results fixes α to be a constant of 2.3 and δ_c as a function of Ω_z (equation 27). The fitted value of α is consistent with both the theoretical work by Navarro, Frenk & White (1996) and observations (Carlberg et al. 1996; Fischer et al. 1997). So, we will adopt the same α derived from GPM to calibrate the PS formalism. But we will adjust δ_c by comparing PS results to N-body results.

The basic PS ansatz results in the differential *virialized halo mass* function as:

$$n(M_v)dM_v = \sqrt{\frac{2}{\pi}} \frac{\bar{\rho}}{M_v} \frac{\delta_c}{\sigma_0^2(M_v)} \frac{d\sigma_0(M_v)}{dM_v} \exp\left(-\frac{\delta_c^2}{2\sigma_0^2(M_v)}\right) dM_v, \quad (32)$$

where $\bar{\rho}$ is the mean density of the universe at the redshift under consideration. Substituting M_v by M_A using equation 14 with $\alpha = 2.3$ gives

$$n(M_A)dM_A = 4.945 \times 10^{15} r_A^{0.913} \Omega_z^{0.173} \Omega_0^{1.304} M_A^{-1.304} \frac{\delta_c}{\sigma_0^2(M_A)} \frac{d\sigma_0(M_A)}{dM_A} \exp\left(-\frac{\delta_c^2}{2\sigma_0^2(M_A)}\right) dM_A. \quad (33)$$

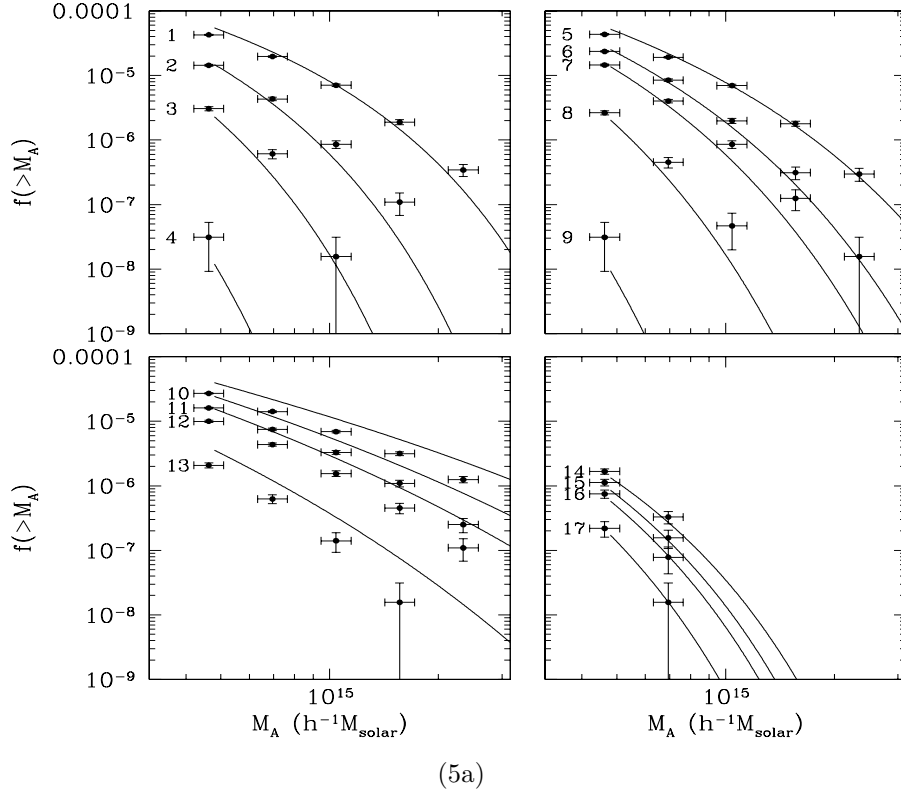


Figure 5a

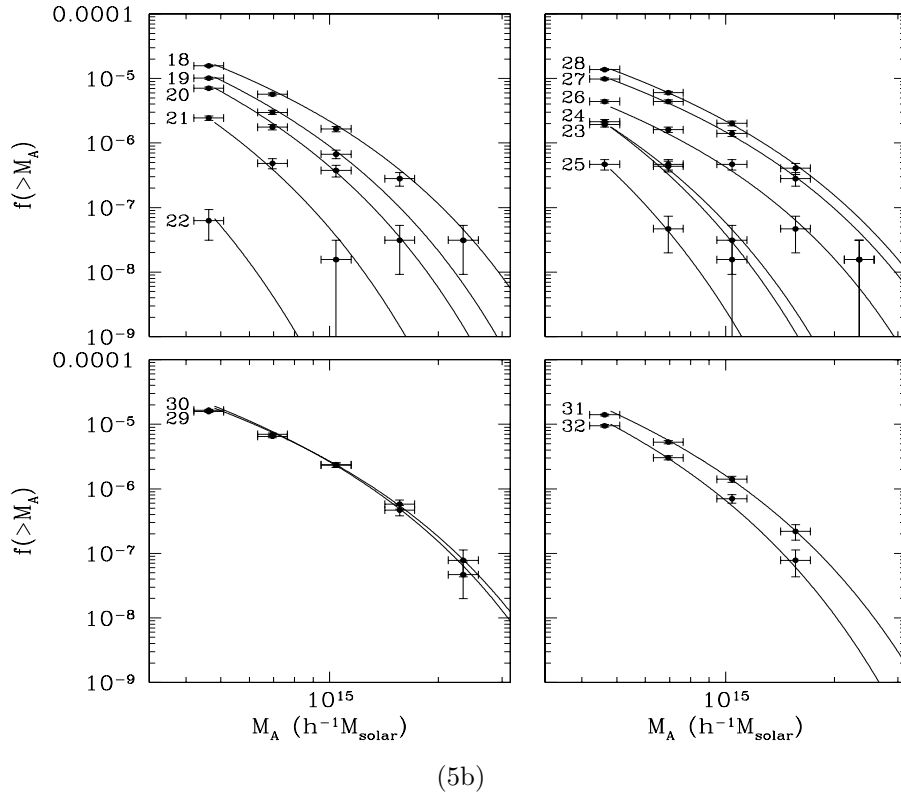


Figure 5b

FIG. 5.— Mass functions of various models. The simulation results are shown as symbols with horizontal errorbars being the uncertainties in the mass determination (15%) and the vertical errorbars being the statistical 1σ errorbars for the number of clusters. The solid curves are the results from Press-Schechter method.

To calculate $\sigma_0(M_A)$ in the above equation we use the *Gaussian* smoothing window with the radius determined by equation 13. The original PS formalism was based on the sharp k-space filter, but it has been shown subsequently by many authors that Gaussian filter works at least as well. The additional virtue of a Gaussian window is that it guarantees a convergent integral for σ_0 for any plausible power spectrum. Now, the only parameter left undetermined is δ_c , which will be fixed by comparing to N-body results. We find that the best overall fit of PS results to N-body results is obtained, if

$$\delta_c = \begin{cases} 1.23 - 0.05(1.0 - \Omega_z) & \text{for } \Lambda_z = 0 \\ 1.23 - 0.01(1.0 - \Omega_z) & \text{for } \Omega_z + \Lambda_z = 1. \end{cases} \quad (34)$$

The results are shown in Figure 5. We see that PS fits N-body results quite well except for the $P_k = k^{-2}$ models (models 10,11,12,13). The PS results for all the $\Omega_0 = 1$ models except the $P_k = k^{-2}$ models appear to be somewhat above the N-body results at the low mass end ($\sim 5 \times 10^{14} h^{-1} M_\odot$) and somewhat below the N-body results at the high mass end ($\sim 2.5 \times 10^{15} h^{-1} M_\odot$). On the other hand, the PS results for all the $P_k = k^{-2}$ models are significantly above the N-body results. So, there is no room for further adjustments of δ_c to achieve better overall fits, at least for Gaussian smoothing windows.

Note that δ_c (~ 1.23) is smaller than 1.67, which is in the expected direction because a smoother, Gaussian smoothing window is used here. 1.23 is also somewhat smaller than that given by Klypin et al. (1995), who give $\delta_c = 1.40$ for a Gaussian smoothing window in the context of damped Lyman alpha systems. But Klypin et al. also argue that δ_c could be as low as 1.3, were waves longer and shorter than those present in the simulation box included. We suspect that δ_c also depends on the shape of the power spectrum in a way that is analogous to the difference between different smoothing windows: a steeper power spectrum (i.e., n being smaller with $P_k = k^n$), which conspires to form a sharp k-space filter like that used in the original derivation of PS, requires a larger δ_c , while a flatter power spectrum requires a smaller δ_c . With this conjecture, the trend that applications of PS to smaller cosmic objects tend to require larger δ_c would have been predicted, since CDM-like spectra have a slowly bending shape which is flatter at small k (i.e., for larger systems) and steeper at large k (i.e., for smaller systems). This conjecture seems to be borne out in the subsequent analyses, as best summarized as in equation 36, where the dependence of σ_8 on Γ is consistent with the above hypothesis. This issue will be addressed elsewhere in more detail.

While PS works well for CDM-like models for computing halo mass functions, consistent with earlier works (Efstathiou & Rees 1988; WEF; ECF), it seems that GPM fits somewhat better the N-body results for CDM-like models and also works for other models tested. An additional advantage is that GPM allows for a determination of the correlation function as well. Therefore, in subsequent calculations we will use GPM, if deemed appropriately applicable.

3. VARIOUS FACTORS THAT AFFECT CLUSTER MASS FUNCTION

It is worthwhile to understand what factors are relevant for the cluster mass function. We begin by show-

ing the cluster mass functions for six variants of the standard CDM model (Table 2 below), as indicated in panels (a,b,e,f,g,h) of Figure 6, at different normalization amplitudes (σ_8). We will return to Table 2 in §4 to discuss the various models in detail. The primordial power spectrum index is assumed to be $n = 1$ for the shown models in panels (a,b,e,f,g,h). Also shown as symbols are the observations adopted from BC, and as three dashed curves are the fits to the symbols. The middle dashed curve is

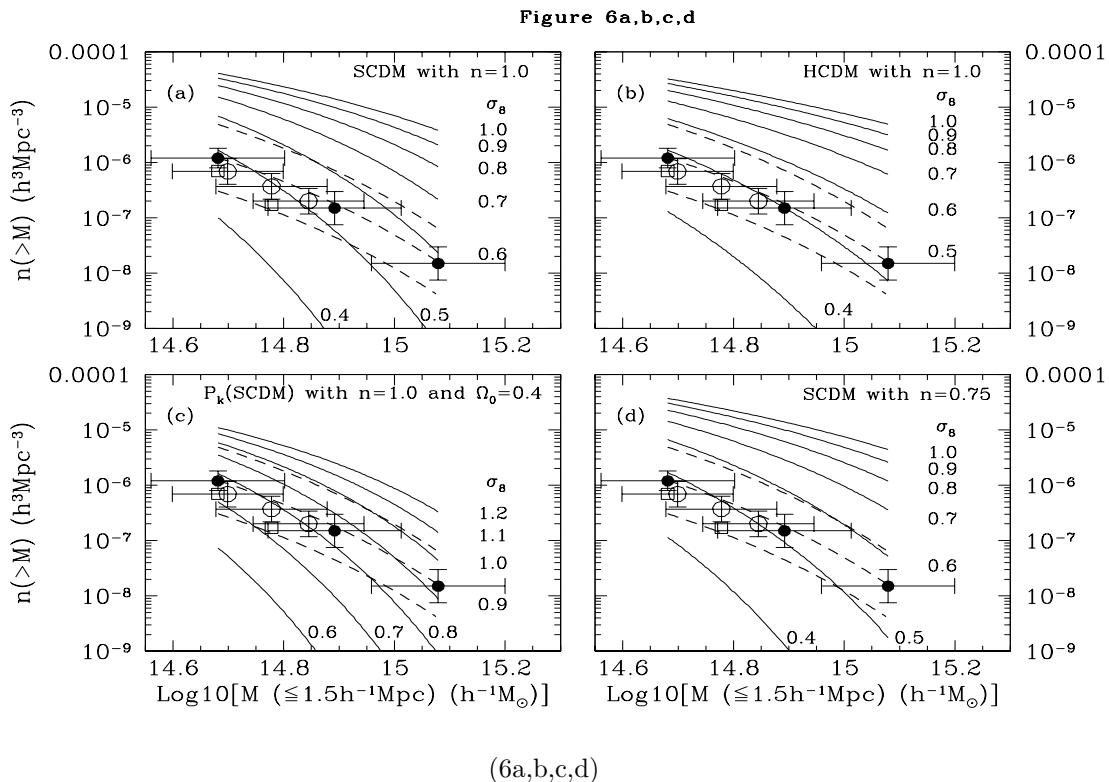
$$n_{fit}(> M_A) = 2.7 \times 10^{-5} (M_A / 2.1 \times 10^{14})^{-1} \exp(-M_A / 2.1 \times 10^{14}), \quad (35)$$

where n_{fit} is in $h^3 \text{Mpc}^{-3}$ and M_A is the cluster mass within the Abell radius in $h^{-1} M_\odot$. This curve seems to represent the mean value of the observed mass function well (note that equation 35 is slightly different from the fitting formula in BC). The top and bottom dashed curves are $4n_{fit}(> M_A)$ and $0.25n_{fit}(> M_A)$. It is difficult to estimate the errorbars of the observed mass function. The top and bottom dashed curves are intended to serve as 2σ upper and lower bounds (in the vertical axis) of the observed mass function within the indicated mass range, which we deem to be conservative. Subsequent presentations and explanations will follow this assertion.

In all cases, we see that the cluster mass function becomes progressively steeper at the high mass end as the amplitude of the density perturbations decreases. The physics behind this is simple to understand. As the amplitude of fluctuations decreases, the required height of the density peaks for clusters with a given mass increases. Since the abundance of the high peaks at the very high end drops exponentially, the mass function steepens as the amplitude of fluctuations decreases. Note that there is only a narrow range in σ_8 where the model mass function lies within the 2σ limits in the mass range from $4.8 \times 10^{14} h^{-1} M_\odot$ to $1.2 \times 10^{15} h^{-1} M_\odot$.

Although it is clear that the amplitude of the power spectrum sensitively determines the abundance of the clusters, as seen by comparing different curves within each panel, it is not yet clear how big the effect of Ω_0 on the mass function is. In Figure 6, panel (c) is similar to panel (a) with only one change: $\Omega_0 = 0.4$ instead of $\Omega_0 = 1.0$. Note that the power spectrum used in panel (c) is identical to that used in panel (a). We see Ω_0 has a significant effect on the mass function. For example, the $\sigma_8 = 1.0$ model in panel (c) has comparable mass function to the $\sigma_8 = 0.6$ model in panel (a), but about two orders of magnitudes lower than the $\sigma_8 = 1.0$ model in panel (a).

Next, we examine the effect of the shape of the power spectrum on the shape of the mass function. In Figure 6 panel (d) is similar to panel (a) but with $n = 0.75$ instead of $n = 1.0$. Comparing panel (d) with panel (a) illustrates the sensitivity of the cluster mass function on the shape of power spectrum. The model shown in panel (d) has substantially more power on large scales ($100 - 300 h^{-1} \text{Mpc}$) than the model shown in panel (a). This difference results in flatter mass functions in panel (d) than in panel (a), especially for the cases with lower σ_8 . A point that we would like to make here is that the cluster mass function depends not only on Ω , Λ and σ_8 , but on P_k in a nontrivial, albeit relatively weak, way, especially at the high mass end of



the mass function. For example, at $1.2 \times 10^{15} h^{-1} M_{\odot}$, the model shown in panel (d) has about a factor of four more clusters than the model shown in panel (a), with the only difference between the two models being a slight tilt of the power spectrum [$n = 0.75$ in (d) vs $n = 1.0$ in (a)].

Panels (e,g) and panels (f,h) show two pairs of low density models, one being open and the other being flat with a cosmological constant but with a same Ω_0 in each pair. One thing to note is that, other things being fixed, the cosmological constant does not make much difference in terms of the shape of the mass function. However, for a fixed σ_8 , the mass function in the model with a cosmological constant is systematically lower than that of the model without a cosmological constant; the difference becomes larger at lower amplitudes.

Summarizing the above results we see that the factors that effect the cluster mass function in order of decreasing importance are σ_8 , Ω_0 , P_k and Λ_0 . The ordering of the last two factors is somewhat more complex; the P_k factor is more significant at the high mass end, whereas the Λ_0 factor affects rather uniformly across-the-board. It is therefore clear that the tightest constraint may be obtained for σ_8 for a given model with Ω_0 , Λ_0 and P_k being specified.

4. NORMALIZING ALL CDM MODELS

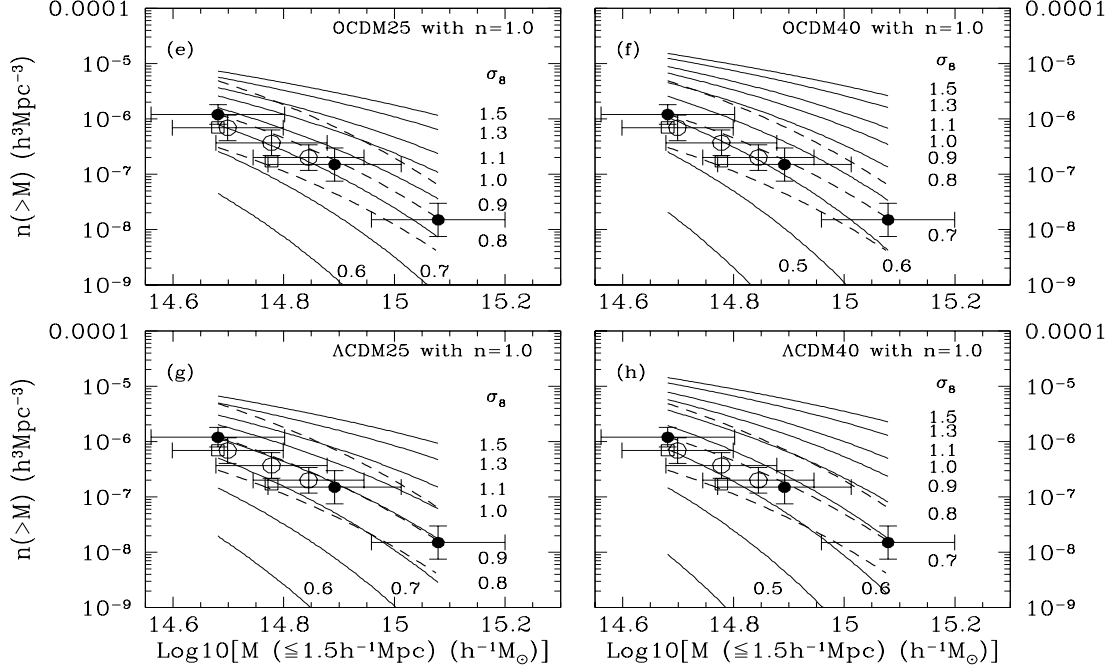
In §2.1 and 2.2 we have shown that the Gaussian peaks of cluster size indeed form clusters of galaxies and appropriately identified peaks reproduce both cluster mass function and cluster two-point correlation function accurately. We now use the observed zero redshift rich cluster abundance and the COBE observation to constrain six repre-

sentative variants of the standard CDM model, which are of current interest. The models are listed in Table 2.

The baryon densities for Models C,E are computed using $\Omega_b h^2 = 0.0125$ (Walker et al. 1991), and for Models A,B,D,F using $\Omega_b h^2 = 0.0193$ (Burles & Tytler 1997). These choices of Ω_b for the models serve to maximize the viability of each model with respect to the observed gas fraction in X-ray clusters of galaxies (White et al. 1993; Lubin et al. 1996; Danos & Pen 1998, $\rho_{gas}/\rho_{tot} = (0.053 \pm 0.004)h^{-3/2}$). The power spectrum transfer functions for all the models are computed using the CMBFAST code developed by Seljak and Zaldarriaga. The choice of the Hubble constant is made for each model such that each model is consistent with current measurements of the Hubble constant. It appears to be a consensus that $H_0(obs) = 65 \pm 10 \text{ km/s/Mpc}$ can account for the distribution of the current data from various measurements (see, e.g., Trimble 1997), except for those from Sunyaev-Zel'dovich observations (for a discussion of a reconciliation of this difference, see Cen 1998). Another consideration is that the age constraint from latest globular cluster observations/interpretations (c.f., Salaris, Degl'Innocenti, & Weiss 1997) is not violated.

The SCDM model (# 1 in Table 2) is the standard CDM with critical density. The mixed hot and cold dark matter model (HCDM) has critical density but with 20% of the mass in light massive neutrinos (two species of equal mass neutrinos are assumed). The next two models, OCDM25 and OCDM40 (# 3 and 4), are open models with matter density of $\Omega_0 = 0.25$ and 0.40 , respectively. The last two models, Λ CDM25 and Λ CDM40 (# 5 and 6), are spatially flat models with the addition of a cosmological constant

Figure 6e,f,g,h



(6e,f,g,h)

FIG. 6.— Cluster mass functions for six models at several different normalization amplitudes of the power spectra. Also shown as symbols are the observations adopted from BC, and as three dashed curves are the fits to the symbols. The solid dots represent the cluster mass function from Abell cluster catalog, the open squares from the Edinburgh-Durham Cluster Catalog (Lumsden et al. 1992), and the open circles from the observed temperature function of Henry & Arnaud (1991). The middle dashed curve is computed by equation 35, $n_{fit}(>M)$, which represents the mean value of the observed mass function well. The top and bottom dashed curves are $4n_{fit}(>M)$ and $0.25n_{fit}(>M)$, respectively.

TABLE 2
SIX VARIANTS OF CDM MODELS

Model Family	Ω_c	Ω_b	Λ_0	H_0	Ω_b	t_{age} (Gyrs)
A	0.936	0.000	0.000	55	0.064	11.8
B	0.736	0.200	0.000	55	0.064	11.8
C	0.220	0.000	0.000	65	0.030	12.4
D	0.346	0.000	0.000	60	0.054	12.7
E	0.220	0.000	0.750	65	0.030	15.2
F	0.346	0.000	0.600	60	0.054	14.5

but with otherwise similar parameters to the two open models. Note that for all models, σ_8 and n are yet to be specified, as will be shown below, by normalizing each model to both COBE and zero redshift cluster abundance.

GPM makes possible economically sample large (four dimensional) parameter space spanned by the uncertainties in Ω_0 , Λ_0 , σ_8 and P_k (the Hubble constant constitutes yet another dimension of uncertainty but its effect can be absorbed into P_k in this case since the final quantities can all be expressed in units of h). The dependence on Ω_b is secondary and ignored here. If the cluster mass function of a model at any mass does not lie within the range delimited by the upper and lower dashed curves in Figure 6 in the mass range from $4.8 \times 10^{14} h^{-1} M_\odot$ to $1.2 \times 10^{15} h^{-1} M_\odot$, we conclude that the model is ruled out at 2σ confidence level (this adoption of confidence level on the mass function is somewhat crude but we think it is perhaps conservative). Thus, we can constrain the $(\Omega_0, \Lambda_0, \sigma_8, P_k)$ four dimensional parameter space by *the cluster mass function*. The other, tight constraint currently available is from the COBE observations of the cosmic microwave background fluctuations on large scales. We will combine these two observations to constrain the models.

With Ω_0 and Λ_0 (and the composition of dark matter and baryonic matter) being fixed, the power spectrum transfer function of a model becomes completely deterministic. What is left to be specified is the primordial power spectrum index, n (assuming it is of a power law form). Figures (7a,b,c,d,e) show the constrained two-dimensional parameter space (σ_8, n) for the six models listed in Table 2. The dotted hatched regions are the permitted space in this two-dimensional parameter plane whose cluster mass functions agree with observations at the 2σ confidence level. The solid hatched regions are the constraints provided by COBE on large scales, where the spread in the vertical axis (σ_8 , $\pm 14\%$, 2σ) is due to the statistical uncertainty of the COBE measurements (Bunn & White 1997). We see that a quite tight constraint is obtained in the (n, σ_8) plane. For the four spatially flat models (1,2,5,6) in Table 2, two cases, with and without the tensor mode (gravitational wave) contribution to the CMB fluctuations on COBE scales, are considered. We assume the tensor to scalar ratio $T/S = 7(1 - n)$ for $n < 1$ (Liddle & Lyth 1992; Davis et al. 1992; Crittenden et al. 1993; Stewart & Lyth 1993) and $T/S = 0$ for $n \geq 1$ (Steinhardt 1997, private communications). For the remaining two models (open models; models 3,4 in Table 2) we only consider the case without the tensor mode contribution; it turns out to make no difference in the end whether tensor mode is considered or not, as the values of n in the allowed range are greater than unity. The permitted ranges of n , σ_8 and EP for all the models are tabulated in Table 3 to clearly show their distinctly different ranges for all the models. However, current observations by COBE on n (Gorski et al. 1996; Bennett et al. 1996; Hinshaw et al. 1996; Bunn & White 1997) and by large scale galaxy distribution on EP (Wright et al. 1992; or equivalently by Γ parameter, Maddox et al. 1990; Feldman, Kaiser, & Peacock 1994; Peacock, & Dodd 1994), as indicated as the last two rows in Table 3, while significantly constraining models at 1σ confidence level, do not yet place 2σ confidence level constraint on this set of models.

The values of n and σ_8 for the central model in each

variant of the CDM model are shown as solid dots in six panels of Figure 7. To facilitate further examination of and intercomparison among the models, the parameters of the six central models are given in Table 4. These six models likely bracket all “viable” CDM models of current interest. This is an attempt to set the context for future discussions of CDM models that will share a common standard.

5. $\sigma_8 - \Omega_0$ RELATION

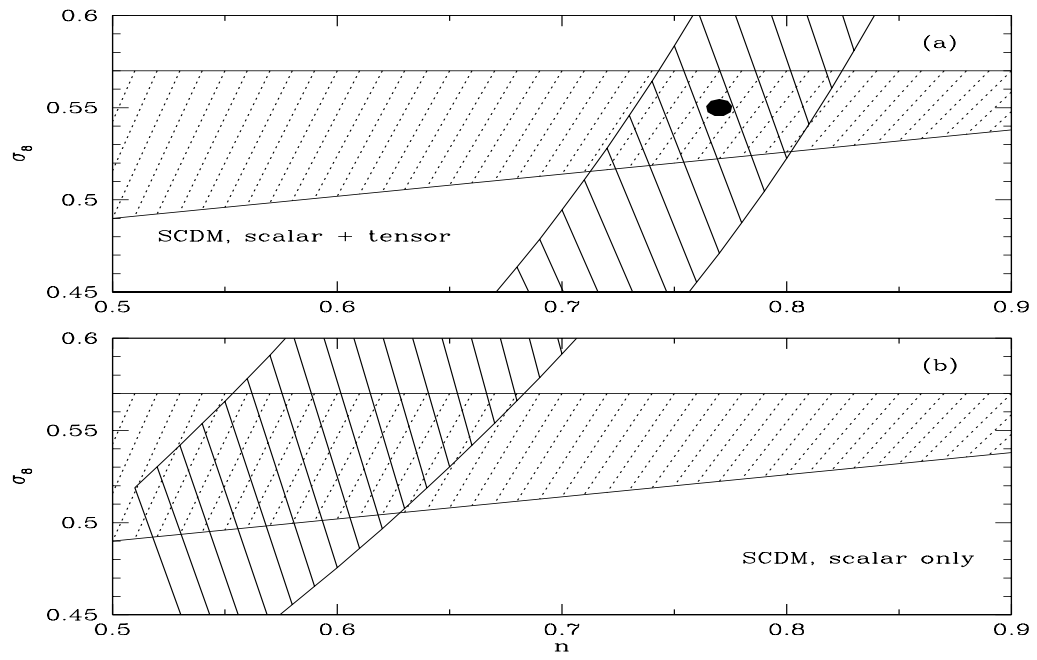
Let us now steer off the main course for a moment and examine the $\sigma_8 - \Omega_0$ relation that has been widely utilized (WEF; Viana & Liddle 1996; ECF). We first note that it is very clear from Figure 7 and Table 3 that the shape of the power spectrum plays a significant role. While we find that the power spectrum shape dependence of σ_8 for $\Omega_0 = 1$ models (Models A,B in Table 3) is modest $\Delta\sigma_8 \sim 0.03 - 0.1$, in agreement with ECF, the power spectrum shape dependence of σ_8 for low density models is substantial, being $\Delta\sigma_8 = 0.17 - 0.30$. Therefore, a more accurate relation of $\sigma_8 - \Omega_0$ cannot be obtained until the shape of the power spectrum is more accurately fixed. The latter is currently unavailable, as indicated by the last two rows of Table 3. A tentative solution to circumvent this situation is to choose a shape of the power spectrum that is deemed to best fit observations of large-scale galaxy distribution. This approach was used by WEF, Viana & Liddle (1996) and ECF, which will also be adopted here.

Figure 8 shows the constraint on the (Ω_0, σ_8) plane, for two cases: $\Gamma = 0.25$ and $\Lambda_0 = 0$ (8a) and $\Gamma = 0.25$ and $\Omega_0 + \Lambda_0 = 1$ (8b). The dotted region in each figure represents the permitted regions of parameters where models have the cluster mass functions at $z = 0$ consistent with the observations at 2σ confidence level. The hatched region is the fit by ECF at 2σ confidence level and the dotted curve is the fit by Viana & Liddle (1996). The dashed curve in (8b) is the fit by WEF. The solid curve is the best fit to the dotted region. The general agreements between various studies are very good. The small differences between the results of various studies perhaps reflect the differences in the procedures of fitting to observational data points, the small differences in the adopted observations being fit, and different theoretical approximations used for the models. Our best fit to the results of GPM to the observed mass function of BC, for $\Gamma = 0.25$, is (2σ) : $\sigma_8(\Omega_0) = (0.52_{-0.05}^{+0.04})\Omega_0^{-0.39}$ for $\Lambda_0 = 0$ and $\sigma_8 = (0.52_{-0.05}^{+0.04})\Omega_0^{-0.43}$ for $\Omega_0 + \Lambda_0 = 1$.

Given the sizable allowed range in Γ currently constrained by observation (Peacock & Dodds 1994), $\Gamma = 0.23_{-0.03}^{+0.04}$ (2σ), it is useful to quantify the dependence of the above relationships on the shape of the power spectrum. Figure 8c shows the results and fits to them for $\Gamma = 0.20$ and $\Gamma = 0.27$, with the best fits being (2σ) $\sigma_8(\Omega_0) = (0.485_{-0.05}^{+0.04})\Omega_0^{-0.39}$ for $\Lambda_0 = 0$ and $\sigma_8 = (0.485_{-0.05}^{+0.04})\Omega_0^{-0.43}$ for $\Omega_0 + \Lambda_0 = 1$ for $\Gamma = 0.20$, and $\sigma_8(\Omega_0) = (0.52_{-0.04}^{+0.05})\Omega_0^{-0.39}$ for $\Lambda_0 = 0$ and $\sigma_8 = (0.52_{-0.04}^{+0.05})\Omega_0^{-0.43}$ for $\Omega_0 + \Lambda_0 = 1$ for $\Gamma = 0.27$. The best fit of all the results for CDM-like models, allowing Γ to vary within the indicated range (0.20 – 0.27), is (2σ) :

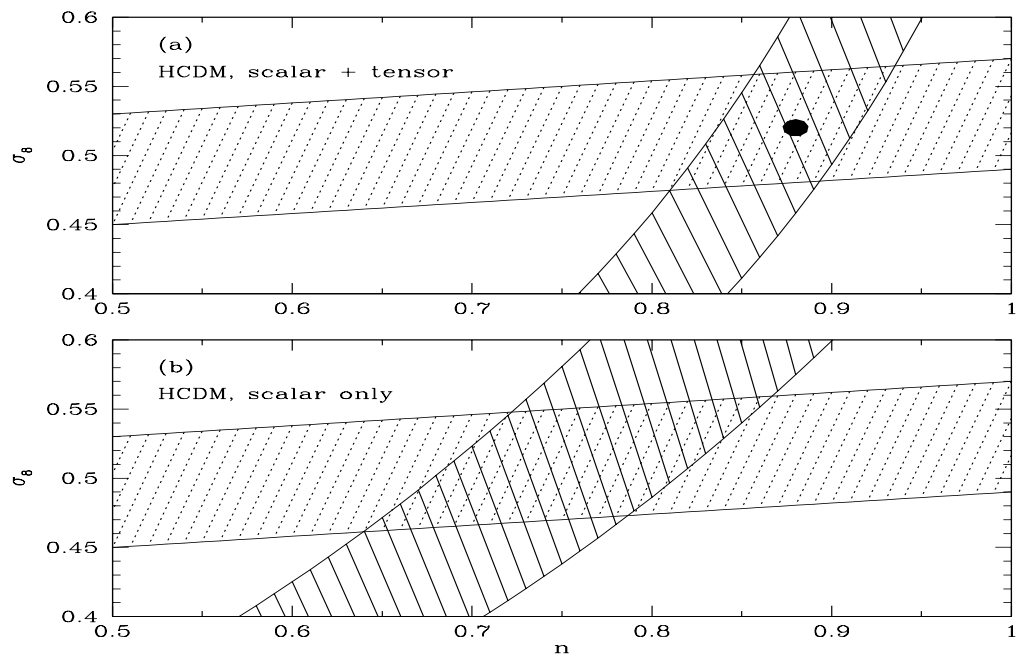
$$\sigma_8(\Omega_0, \Gamma) = \begin{cases} [(0.50 + 0.5(\Gamma - 0.23) \pm 0.05)\Omega_0^{-0.39}] & (\Lambda_0 = 0) \\ [(0.50 + 0.5(\Gamma - 0.23) \pm 0.05)\Omega_0^{-0.43}] & (\Omega_0 + \Lambda_0 = 1) \end{cases} \quad (36)$$

Figure 7a



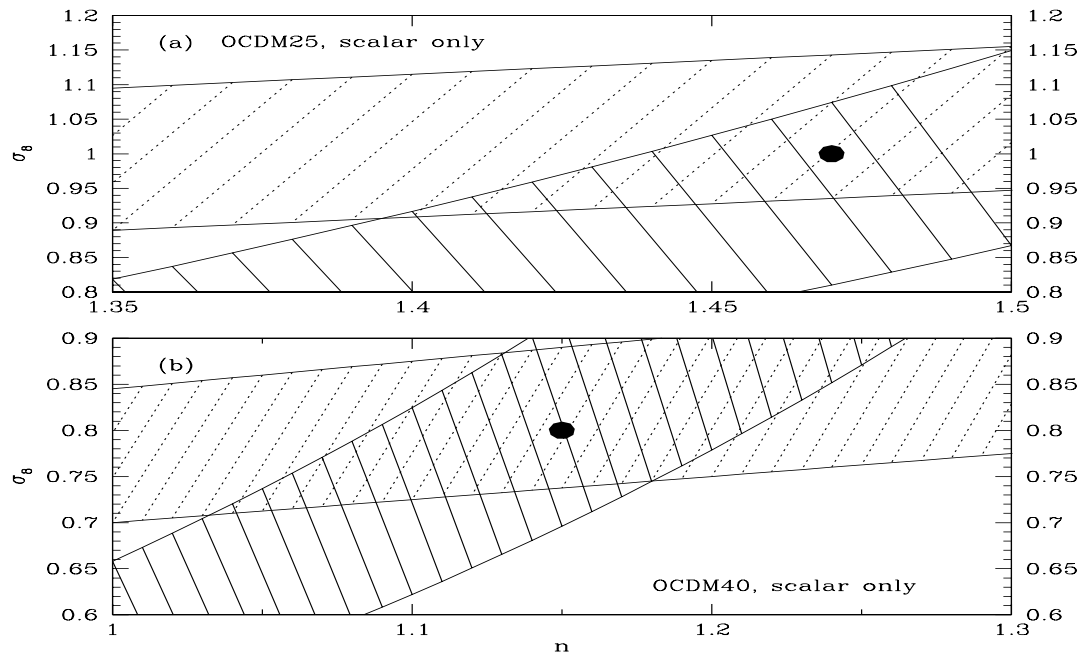
(7a)

Figure 7b



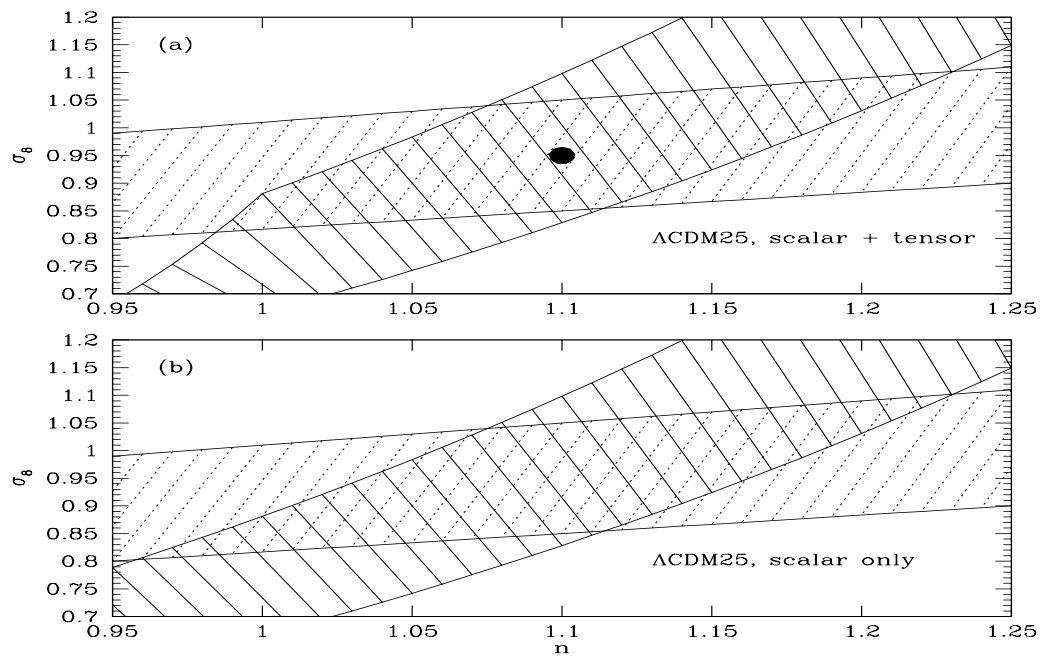
(7b)

Figure 7c



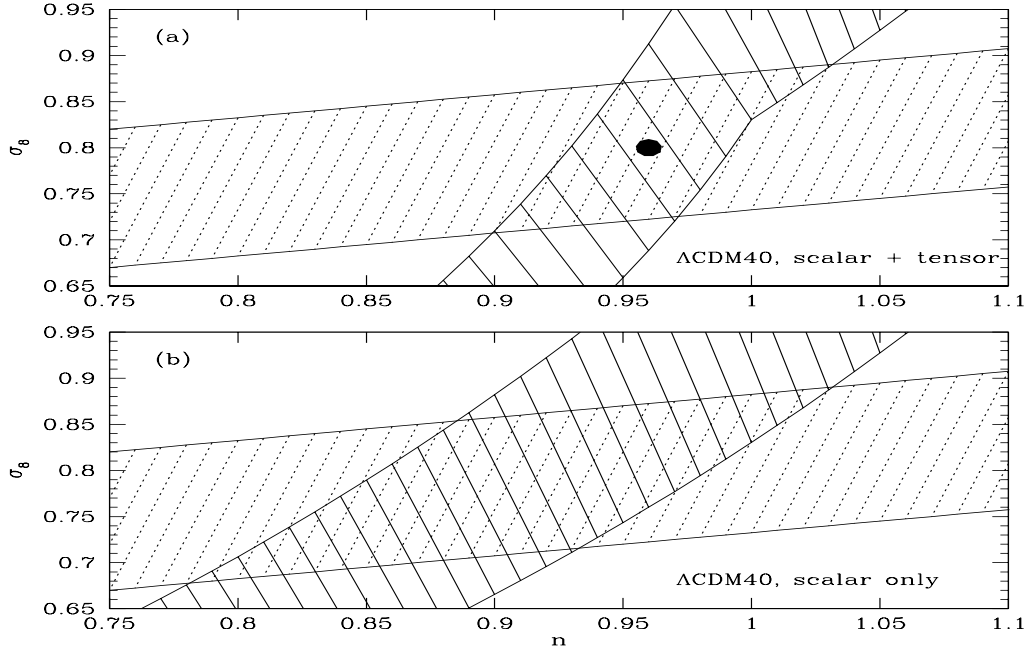
(7c)

Figure 7d



(7d)

Figure 7e



(7e)

FIG. 7.— The constrained two-dimensional parameter space (σ_8, n) for the six models as tabulated in Table 2. The dotted hatched regions are the permitted space in this two-dimensional parameter plane whose cluster mass functions agree with observations at the 2σ confidence level. The solid hatched regions are the constraints provided by COBE on large scales, where the spread in the vertical axis $(\sigma_8, \pm 14\%, 2\sigma)$ is due to the statistical uncertainty of the COBE measurements (Bunn & White 1997). For the four spatially flat models (models 1,2,5,6) two cases, with and without the tensor mode (gravitational wave) contribution to the CMB fluctuations on COBE scales are considered (see text). For the remaining two models (open models; models 3,4 of Table 2) we only consider the case without the gravitational wave contribution.

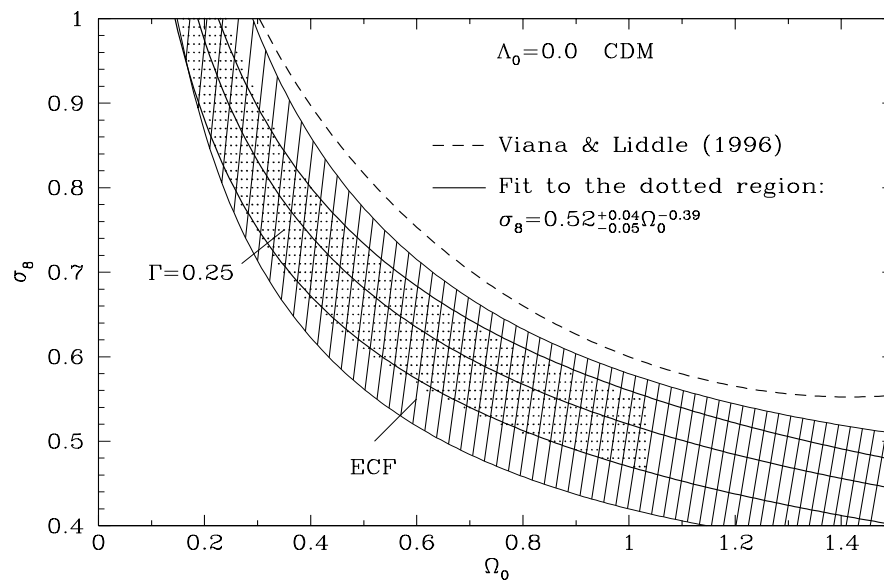
TABLE 3
CONSTRAINTS ON n , σ_8 AND EP FOR THE SIX VARIANTS OF TABLE 2

Model Family	Tensor mode	n range	σ_8 range	EP range
A	yes	0.72 – 0.82	0.52 – 0.57	1.01 – 1.05
A	no	0.45 – 0.68	0.49 – 0.52	1.07 – 1.20
B	yes	0.79 – 0.92	0.45 – 0.54	1.44 – 1.53
B	no	0.61 – 0.84	0.43 – 0.53	1.49 – 1.65
C	no	1.39 – 1.49	0.91 – 1.14	1.11 – 1.16
D	no	0.98 – 1.23	0.64 – 0.84	1.25 – 1.40
E	yes	0.98 – 1.23	0.81 – 1.10	1.25 – 1.40
E	no	0.96 – 1.23	0.80 – 1.10	1.25 – 1.42
F	yes	0.87 – 0.99	0.65 – 0.82	1.40 – 1.47
F	no	0.74 – 0.98	0.62 – 0.81	1.40 – 1.56
COBE(obs)	-	1.20 ± 0.60 (2σ)	-	-
LSS(obs)	-	-	-	1.30 ± 0.30 (2σ)

TABLE 4
SIX COBE AND CLUSTER-NORMALIZED CDM MODELS

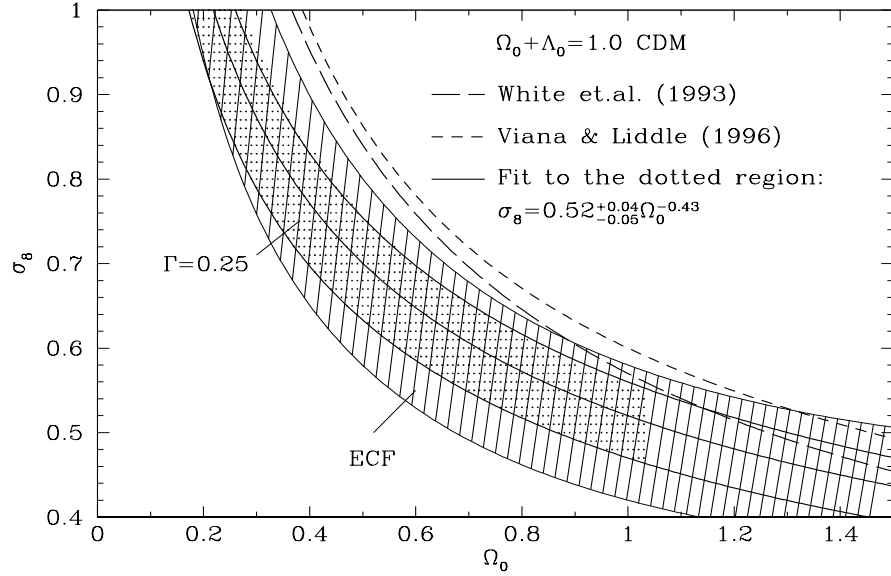
Model	H_0	n	Ω_c	Ω_b	Λ_0	Ω_m	σ_8
tCDM	55	0.77	0.936	0.00	0.0	0.064	0.55
HCDM	55	0.88	0.736	0.20	0.0	0.064	0.52
OCDM25	65	1.47	0.220	0.00	0.0	0.030	1.00
OCDM40	60	1.15	0.346	0.00	0.0	0.054	0.80
Λ CDM25	65	1.10	0.220	0.00	0.75	0.030	0.95
Λ CDM40	60	0.96	0.346	0.00	0.60	0.054	0.80

Figure 8a

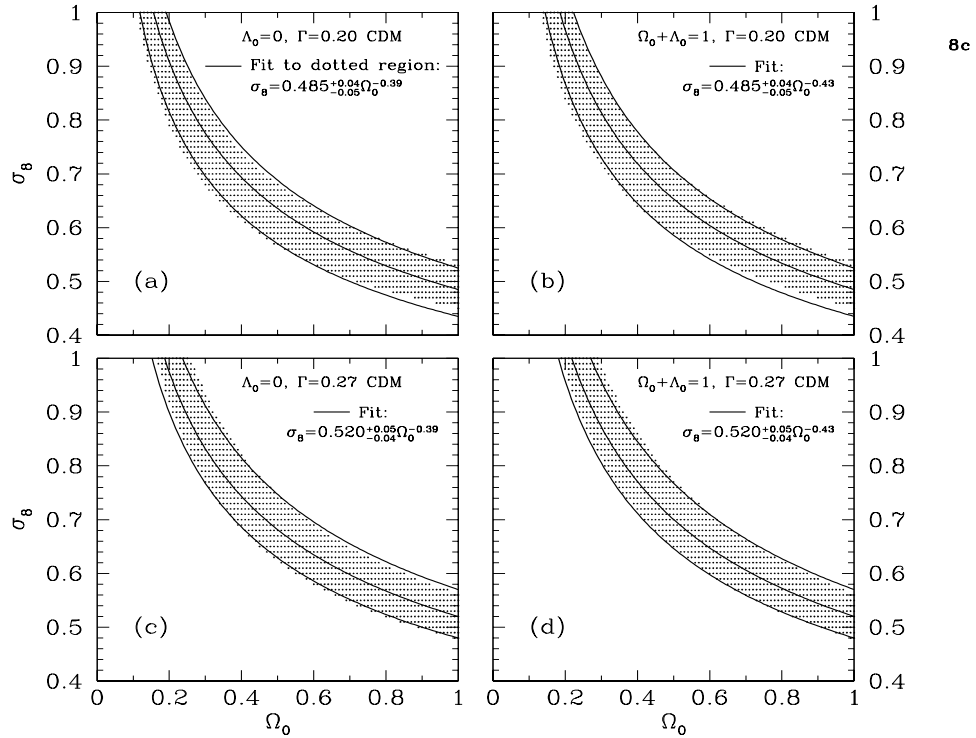


(8a)

Figure 8b



(8b)



(8c)

FIG. 8.— The constraint on the (Ω_0, σ_8) plane, for two cases: $\Gamma = 0.25$ and $\Lambda_0 = 0$ (8a) and $\Gamma = 0.25$ and $\Omega_0 + \Lambda_0 = 1$ (8b). The dotted region in each figure represents the permitted regions of parameters whose models have the cluster mass functions at $z = 0$ consistent with what is observed at 2σ confidence level. The hatched region is the fit by Eke et al. (1996) at 2σ confidence level and the short-dashed curve is the fit by Viana & Liddle (1996). The long-dashed curve is the fit by White et al. (1993). The solid curve is the best fit to the dotted region with the fitting formula being indicated in the figure. Figure 8c shows the results and fits to them for $\Gamma = 0.20$ and $\Gamma = 0.27$. The best fit of the results, allowing Γ to vary within the indicated range, is presented in equation 36.

This $\sigma_8 - \Omega_0$ relation best summarizes a constraint on CDM-like models provided by the observations of zero redshift rich cluster abundance.

6. CONCLUSIONS

We have developed and tested a method to compute the mass function and correlation function of peaks, based on the formalism for Gaussian density field. We should call this method Gaussian Peak Method (GPM). The essential new ingredient in this relatively old method is a simultaneous determination of the smoothing window size (to select appropriate peaks) and the critical peak height of collapse. A large set of thirty-two N-body simulations are used to test the accuracy of the method and it is shown that the method is accurate for all the models tested, which cover the parameters space of interest spanned by P_k , Ω_0 , Λ_0 and σ_8 .

The GPM permits economical search of parameter space. We find that $\sigma_8 - \Omega_0$ relation is somewhat dependent upon the shape of the power spectrum. Normalizing CDM models to the observed local rich cluster abundance *alone*, allowing for the observed uncertainty in the shape parameter $\Gamma(\equiv \Omega_0 h) = (0.20 - 0.27)$, gives (2σ) :

$$\sigma_8(\Omega_0, \Gamma) = \begin{cases} [0.50 + 0.5(\Gamma - 0.23) \pm 0.05] \Omega_0^{-0.39} & (\Lambda_0 = 0) \\ [0.50 + 0.5(\Gamma - 0.23) \pm 0.05] \Omega_0^{-0.43} & (\Omega_0 + \Lambda_0 = 1) \end{cases} \quad (37)$$

Matching both COBE on very large scales and the abundance of local rich clusters of galaxies fixes both the shape (n) and amplitude of the power spectrum (σ_8) of any model to about 10% accuracy. Consequently, all models become almost completely deterministic. A set of six CDM models (including cold plus hot dark matter model) (Table 4), likely bracketing all potentially interesting models, is advertized together. This should be viewed as an attempt to set the context for future discussions on a set of standardized models to facilitate comparison of results between workers in the field.

The work is supported in part by grants NAG5-2759 and ASC93-18185. Discussions with Drs. N. Bahcall, J.R. Bond, X. Fan, F. Governato, G. Lake, J.P. Ostriker and D. Scott are gratefully acknowledged. I thank Dr. F.J. Summers for allowing me to use his P³M simulation to calibrate the simulation resolution, and Drs. U. Seljak and M. Zaldarriaga for making the CMBFAST code available. Finally, I would like to thank George Lake and University of Washington for the warm hospitality, and financial support from the NASA HPCC/ESS Program during a visit when this work was initiated. The program to compute cluster mass and correlation function is available upon request by sending email to cen@astro.princeton.edu.

REFERENCES

- Albrecht, A. & Steinhardt, P.J. 1982, Phys. Rev. Lett., 48, 1220
 Bahcall, N.A. 1988, ARAA, 26, 631
 Bahcall, N.A., & Cen, R. 1992, ApJ, 398, L81
 Bahcall, N.A., & Cen, R. 1993, ApJ, 407, L49 (BC)
 Bahcall, N.A., & Soneira, R.M. 1983, ApJ, 270, 20
 Bahcall, N.A., Fan, X., & Cen, R. 1997, ApJ, 485, L53
 Bardeen, J.M., Steinhardt, P.J., & Turner, M.S. 1983, Phys. Rev. D, 28, 679
 Bardeen, J.M., Bond, J.R., Kaiser, N., & Szalay, A.S. 1986, ApJ, 304, 15.
 Bardeen, J.M., Bond, J.R., & Efstathiou, G. 1987, ApJ, 321, 28
 Barriola, M. & Vilenkin, A. 1989, Phys. Rev. Lett., 63, 341
 Bartlett, J.G., & Silk, J. 1993, ApJ, 407, L45
 Baugh, C.M., Gaztanaga, E., & Efstathiou, G. 1995, MNRAS, 274, 1049
 Bennett, C.L., et al. 1996, ApJ, 464, L1
 Bennett, D.P., & Rhie, S.H. 1990, Phys. Rev. Lett., 65, 1709
 Bond, J.R., & Couchman, H.M.P. 1988, in Proc. Second Canadian Conference on General Relativity & Relativistic Astrophysics, eds. A. Coley, C.C. Dyer, & B.O.J. Tupper (Singapore: World Scientific), 385
 Borgani, S., Plionis, M., Coles, P., & Moscardini, L. 1995, MNRAS, 277, 1191
 Brieu, P., Summers, F.J., & Ostriker, J.P. 1995, ApJ, 453, 566
 Bunn, E.F., & White, M. 1997, ApJ, 480, 6
 Bucher, Goldhaber, & Turok, N. 1995, preprint
 Burles, S., & WTytler, D. 1997, preprint, astro-ph/9712108
 Carlberg, R.G., Yee, H.K.C., Ellingson, E., Abraham, R., Gravel, P., Morris, S.M., & Pritchet, C.J., 1996, ApJ, 462, 32
 Postman, M., Lubin, L., Gunn, J.E., Oke, J.G., Schneider, D.P., & Christensen, J.A., 1996, ApJ, 111, 615
 Cen, R. 1997b, ApJ, 485, 39
 Cen, R. 1998, ApJ, in press
 Cen, R., Bahcall, N.A., & Gramann, M. 1994, ApJ, 437, L51
 Colless, M. 1998, preprint, astro-ph/9804079
 Colley, W.N. 1997, ApJ, 489, 471
 Colley, W.N., Gott, J.R., III, & Park, C. 1996, MNRAS, 281, L82
 Crittenden, R., Bond, J.R., Davis, R.L., Efstathiou, G., & Steinhardt, P.J. 1993, Phys. Rev. Lett., 71, 324
 Croft, R.A.C., & Efstathiou, G. 1994, MNRAS, 267, 390
 Croft, R.A.C., Dalton, G.B., Efstathiou, G., Sutherland, W.J., & Maddox, S.J. 1997, MNRAS, 291, 305
 Dalton, G.B., Efstathiou, G., Maddox, S.J., & Sutherland, W.J. 1992, ApJ, 390, L1
 Dalton, G.B., Croft, R.A.C., Efstathiou, G., Sutherland, W.J., Maddox, S.J., & Davis, M. 1994, MNRAS, 271, L47
 Danos, R., & Pen, U. 1998, preprint, astro-ph/9803058
 Davis, M., & Peebles, P.J.E. 1983, ApJ, 267, 465
 Davis, R.L., Hodges, H.M., Smoot, G.F., Steinhardt, P.J., Turner, M.S. 1992, Phys. Rev. Lett., 69, 1856; erratum, 70, 1733
 Dressler, A. 1980, ApJS, 42, 565
 Dressler, A., & Shectman, S.A. 1988, AJ, 95, 985
 Efstathiou, G., & Rees, M. 1988, MNRAS, 230, 5
 Eke, V.R., Cole, S., & Frenk, C.S. 1996, MNRAS, 282, 263 (ECF)
 Einasto, J., Einasto, M., Gottlober, S., Muller, V., Saar, V., Starobinsky, A.A., Tago, E., Tucker, D., Andernach, H., & Frisch, P. 1997, Nature, 385, 139
 Einasto, J., Einasto, M., Frisch, P., Gottlober, S., Muller, V., Saar, V., Starobinsky, A.A., Tago, E., Tucker, D., & Andernach, H. 1997, MNRAS, 289, 801
 Einasto, J., Einasto, M., Frisch, P., Gottlober, S., Muller, V., Saar, V., Starobinsky, A.A., & Tucker, D. 1997, MNRAS, 289, 813
 Feldman, H.A., Kaiser, N., & Peacock, J.A. 1994, ApJ, 437, 56
 Fischer, P., Bernstein, G., Rhee, G., & Tyson, J.A. 1997, AJ, 113, 521
 Geller, M.J. & Beers, T.C. 1982, Publ. Ast ron. Soc. Pac., 94, 421
 Goldberg, D.M., & Strauss, M.A. 1998, ApJ, 495, 29
 Gorski, K.M., Banday, A.J., Bennett, C.L., Hinshaw, G., Kogut, A., Smoot, G.F., & Wright, E.L. 1996, ApJ, 464, L11
 Gott, J.R., III 1982, Nature, 295, 304
 Gunn, J.E., & Gott, J.R. 1972, ApJ, 176, 1.
 Guth, A.H., & Pi, S.-Y. 1982, Phys. Rev. Lett. 49, 1110
 Henry, J.P., & Arnaud, K.A. 1991, ApJ, 372, 410
 Hinshaw, G., et al. 1996, ApJ, 464, L17
 Holtzman, J.A., & Primack, J.R. 1993, ApJ, 405, 428
 Kaiser, N. 1984, ?
 Kaiser, N., & Davis, M. 1985, ApJ, 297, 365
 Klypin, A.A., & Kopylov, A.I. 1983, Soviet Astr. Letters, 9, 41
 Klypin, A., Borgani, S., Holtzman, J., & Primack, J. 1995, ApJ, 444, 1
 Kogut, A., Banday, A.J., Bennett, C.L., Gorski, K.M., Hinshaw, G., & Smoot, G.F. 1996, ApJ, 464, L29
 Lacey, C., & Cole, S. 1993, MNRAS, 262, 627
 Liddle, A.R., & Lyth, D.H. 1992, Phys. Lett., B 291, 391
 Linde, A. 1982, Phys. Lett, 108B, 389
 Lowenthal, J.D., Koo, D.C., Guzman, R., Gallego, J., Phillips, A.C., Faber, S.M., Vogt, N.P., Illingworth, G.D., & Gronwall, C. 1997, ApJ, 481, 673
 Lu, L., Sargent, W.L.W., & Barlow, T.A. 1997, ApJ, 484, 131

- Lubin, L.M., Cen, R., Bahcall, N.A., & Ostriker, J.P. 1996, *ApJ*, 460, 10
- Luppino, G.A., & Gioia, I.M. 1995, *ApJ*, 445, 77 (LG95)
- Maddox, S.J., Efstathiou, G., Sutherland, W.J., & Loveday, J. 1990, *MNRAS*, 242, 43p
- Mann, R.G., Heaven, A.F., & Peacock, J.A. 1993, *MNRAS*, 263, 798
- More, J.G., Heavens, A.F., & Peacock, J.A. 1986, *MNRAS*, 220, 189
- Navarro, J.F., Frenk, C.S., & White, S.D.M. 1996, *ApJ*, 462, 563
- Nichol, R.C., Collins, C.A., Guzzo, L., & Lumsden, S.L. 1992, *MNRAS*, 255, 21p
- Oukbir, J., & Blanchard, A. 1992, *A&A*, 262, L21
- Peacock, J.A., & Dodds, S.J. 1994, *MNRAS*, 267, 1020
- Peacock, J.A., & Heavens, A.F. 1985, *MNRAS*, 217, 805
- Peebles, P.J.E. 1980, *The Large-Scale Structure of the Universe* (Princeton: Princeton University Press)
- Peebles, P.J.E., Daly, R.A., & Juskiewicz, R. 1989, *ApJ*, 347, 563
- Pen, U.-L. 1996, preprint, astro-ph/9610147
- Postman, M., Huchra, J.P., & Geller, M.J. 1992, *ApJ*, 384, 404
- Press, W.H., & Schechter, P.L. 1974, *ApJ*, 215, 703
- Protogeropoulos, Z.A.M., & Weinberg, D.H. 1997, *ApJ*, 489, 457
- Richstone, D., Loeb, A., & Turner, E.L. 1992, *ApJ*, 393, 477
- Romer, A.K., Collins, C.A., Bohringer, H., Cruddace, R.G., Ebeling, H., MacGillivray, H.T., & Voges, W. 1994, *Nature*, 372, 75
- Salaris, M., Degl'Innocenti, S., & Weiss, A. 1997, *ApJ*, 479, 665
- Smoot, G.F. et al. 1992, *ApJ*, 396, L1.
- Stewart, E., & Lyth, D.H. 1993, *Phys. Lett. B*, 302, 171
- Strauss, M.A., & Willick, J.A. 1995, *Phys. Rep.*, 261, 271
- Strauss, M.A., Cen, R., Ostriker, J.P., Lauer, T.R., & Postman, M. 1995, *ApJ*, 444, 507
- Suto, Y., Cen, R., & Ostriker, J.P. 1992, 395, 1
- Trimble, V. 1997, "The Extragalactic Distance Scale" ed. M. Livio, M. Donahue & N. Panagia, p407
- Turok, N. 1989, *Phys. Rev. Lett.*, 63, 2625
- Viana, P.T.P., & Liddle, A.R. 1996, *MNRAS*, 281, 323
- Vilenkin, A. 1981, *Phys. Rev. Lett.*, 46, 1169
- Vilenkin, A. 1985, *Phys. Rep.*, 121, 263
- Vogeley, M.S., Park, C., Geller, M.J., Huchra, J.P., & Gott, J.R., III 1994, *ApJ*, 420, 525
- Walker, T.P. et al. 1991, *ApJ*, 376, 51
- West, M.J., Oemler, A., Jr., & Dekel, A. 1988, *ApJ*, 327, 1
- White, S.D.M., Efstathiou, G., & Frenk, C.S. 1993a, *MNRAS*, 262, 1023 (WEF)
- White, S.D.M., Navarro, J.F., Evrard, A.E., & Frenk, C.S. 1993, *Nature*, 366, 6454
- Wright, E.L., et al. 1992, *ApJ*, 396, L13
- Xu, G. 1995, *ApJS*, 98, 355
- Zel'dovich, Ya. B. 1980, *MNRAS*, 192, 663